

A new angle on stacking faults: Breaking the edge-on limit in high-resolution defect analysis

**Nicolas Karpstein ^a, Lukas Müller ^a, Andreas Bezold ^{b,c},
Steffen Neumeier ^b, Erdmann Spiecker ^{a,*}**

^a Friedrich-Alexander-Universität Erlangen-Nürnberg, Department of Materials Science & Engineering, Institute of Micro- and Nanostructure Research, and Center for Nanoanalysis and Electron Microscopy (CENEM), IZNF, Erlangen, Germany

^b Friedrich-Alexander-Universität Erlangen-Nürnberg, Department of Materials Science & Engineering, Institute I: General Materials Properties, Erlangen, Germany

^c The Ohio State University, Department of Materials Science & Engineering, Columbus, OH, USA

Corresponding author: erdmann.spiecker@fau.de

Abstract

The nature of stacking faults—whether intrinsic or extrinsic—plays a pivotal role in defect-mediated processes in crystalline materials. Yet, current electron microscopy techniques for their reliable analysis remain limited to either conventional fringe-contrast imaging of inclined faults or atomic-resolution imaging of edge-on configurations. Here, we overcome this dichotomy by introducing a high-resolution scanning transmission electron microscopy (HRSTEM) method that enables full structural discrimination of inclined stacking faults in fcc and L1₂ crystals. This approach eliminates a long-standing geometric constraint on high-resolution analysis, providing comprehensive access to stacking faults on all glide planes along the widely used [001] and [110] zone axes. We demonstrate the robustness of the method in a CoNi-based superalloy, achieving clear discrimination of fault types even in overlapping configurations and foil thicknesses exceeding 100 nm. Simulations reveal that fault-induced de-

channeling is key to contrast formation and is strongly governed by the fault's depth within the sample. Leveraging this effect, we further establish a route to artificially generate ultrathin TEM lamellae—bounded by the stacking fault itself—thereby enhancing contrast for atomic-scale studies of long-range ordering, compositional fluctuations, and nanoclustering.

Keywords: fcc; L1₂; stacking faults; scanning transmission electron microscopy; superalloys;

1 Introduction

Stacking faults (SFs) are among the most significant defects in crystalline materials. Since their initial theoretical description and subsequent experimental observation by X-ray diffraction around 1940 [1, 2], SFs have been identified in a broad range of materials, including metals [3], layered crystals [4], and semiconductors [5]. Far from being mere imperfections, SFs can profoundly influence both the structural and functional properties of materials (e.g. [5-7]). While SFs often originate from dislocation glide, they can also arise from the agglomeration of point defects associated with dislocation climb, or form directly during the crystal growth process. Given their diverse origins and significant impact on material behavior, it is therefore essential to characterize SFs reliably and comprehensively across a range of experimental conditions.

SFs are particularly prevalent in close-packed crystal structures. In face-centered cubic (fcc) materials, they play a significant role in governing deformation behavior. When the SF energy is sufficiently low, these planar defects form by the dissociation of dislocations [8], or in larger quantities through mechanisms such as transformation-induced or twinning-induced plasticity [9, 10]. Once present, SFs can act as barriers to further dislocation motion [11, 12]. At elevated temperatures, SFs can also undergo local compositional changes due to atomic-scale Suzuki segregation along the fault plane [13, 14]. Thus, SFs represent a critical microstructural feature in many fcc- or hcp-based alloys.

SF-based deformation mechanisms have received particular attention in γ/γ' -strengthened superalloys with the base element Ni or Co (e.g. [15-26]), which are tailored to possess excellent mechanical properties at temperatures near their melting points [27, 28]. In this class of alloys, the γ matrix phase possesses the fcc structure; coherently embedded into this phase are cuboidal

precipitates of the L1₂-ordered γ' intermetallic phase typically based on a composition of Ni₃Al for Ni-base and Co₃(Al,W) for Co-base superalloys. The interplay between both phases gives rise to a precipitation-strengthening effect, where dislocations face a barrier against entering the precipitates because perfect $\frac{a}{2}\langle 110 \rangle$ dislocations of the γ phase are not perfect in γ' but would create a high-energy antiphase boundary [29]. Furthermore, perfect superdislocations in γ' are energetically unfavorable due to their large Burgers vectors. Thus, dislocation configurations entering the γ' phase often dissociate into partial and superpartial dislocations, leaving behind planar faults including SFs [15, 21, 30]. Besides shearing, SFs in superalloys have also been observed to form through dislocation climb [31]. Depending on alloy composition and deformation parameters, SF-based deformation mechanisms can be responsible for a majority of the plastic deformation in these alloys [32, 33].

For the investigation of crystal defects, (scanning) transmission electron microscopy ((S)TEM) is particularly suitable. A schematic overview of different TEM-based analysis methods to determine the type of a given SF, i.e., whether it is intrinsic (ISF) or extrinsic (ESF), is shown in Fig. 1.

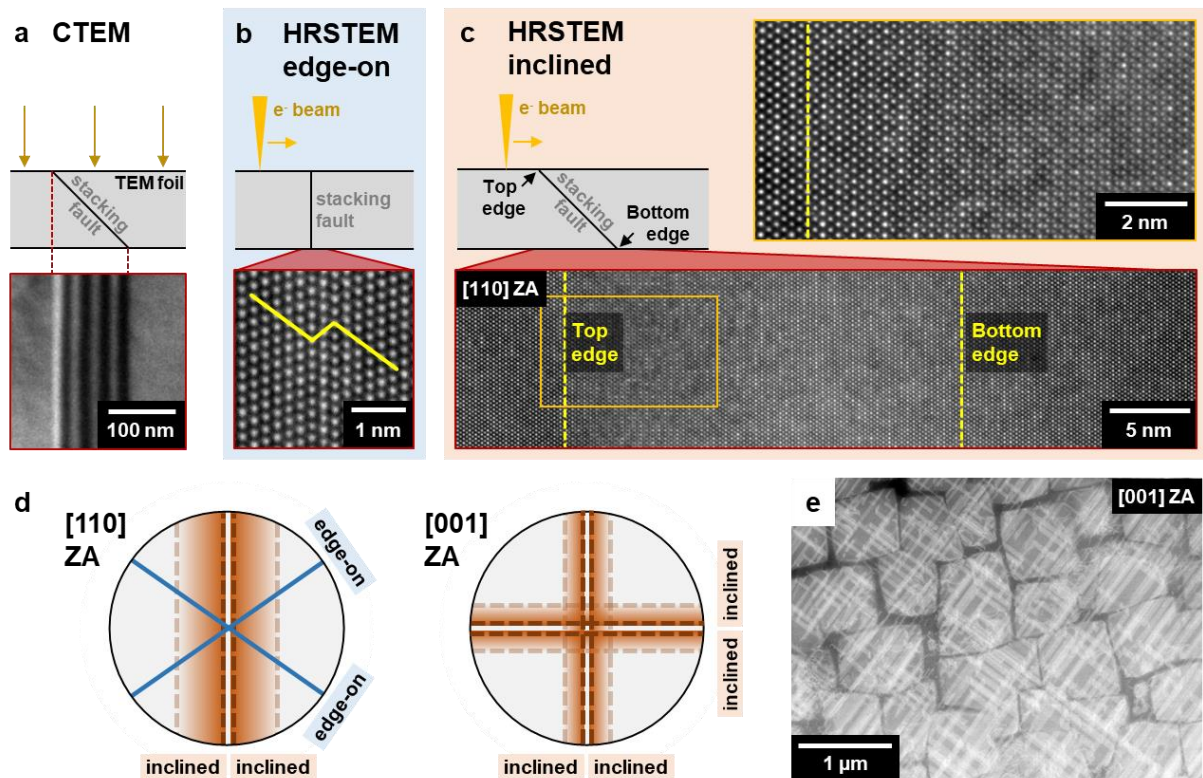


Fig. 1: Schematic overview of different SF analysis methods in the TEM, and crystallographic orientation of SFs in a TEM foil. (a) Conventional fringe-based contrast at inclined SFs. (b) HRSTEM-based method observing the stacking sequence

edge-on. (c) Novel method enabling the HRSTEM-based analysis of inclined SFs. The SF is imaged in the region where it intersects the upper surface of the TEM lamella (top edge). In the example, this occurs on the left side of the image; toward the right, the depth of the SF gradually increases, as shown in the schematic side view. The magnified HRSTEM image of the SF near the top edge reveals a superposition of the lattices above and below the fault, enabling a direct evaluation of the projected lattice shift. (d) Schematic representation of the edge-on or inclined orientations of the $\{111\}$ habit planes of SFs when the crystal is viewed in a $[110]$ or $[001]$ ZA. (e) ADF-STEM micrograph of the microstructure of the ERBOCo-4 alloy after deformation, exhibiting a high SF density.

Methods for determining the types of planar faults in TEM based on fringe contrast (Fig. 1a) have been available for many decades and continue to be applied today [33-36]. In fcc materials, as fringe contrast requires an inclined SF orientation, $[001]$ foils are typically used, where all four $\{111\}$ glide planes are in inclined orientation (Fig. 1d). For instance, the method by Gevers et al. [36] uses a dark-field micrograph under two-beam conditions. The origin of the g vector is placed at the center of the fault, and the fault type is determined based on the nature of the reflection and whether the g vector points toward or away from the bright outer fringe. Since fringe contrast is highly sensitive to small changes in excitation error, it can be challenging to obtain reliable results using these fringe-based methods, especially when the crystal is strongly bent. Additionally, SF analysis becomes difficult when the fault segment is very short or when two or more SFs overlap.

Continuous improvements in high-resolution TEM (HRTEM) and high-resolution STEM (HRSTEM) have enabled more robust analysis of stacking faults (SFs) through the direct interpretation of atomic-scale stacking sequences in micrographs (Fig. 1b) (e.g. [19, 37] for superalloys). This requires the SF to be in edge-on orientation; therefore, in fcc materials, $[110]$ foils are commonly used, where two of the four $\{111\}$ glide planes are edge-on (Fig. 1d). In the $L1_2$ structure, given sufficient superlattice contrast of the atomic columns, it is also possible to determine reliably whether a fault is complex or not [38]. A major limitation of this method is the access to only two of the four glide planes in $[110]$ foils, as the other two are at an inclined angle to the viewing direction, and the complete inadequacy of $[001]$ foils, where all four glide planes are inclined. Schematic drawings of the orientations of the $\{111\}$ SF habit planes in fcc crystals viewed along the $[110]$ and $[001]$ zone axes (ZAs) are shown in Fig. 1d.

To overcome these limitations, in this work, we present a new method enabling the analysis of SFs on inclined planes using HRSTEM (Fig. 1c), combining the advantages of this imaging technique with access to all four glide planes in both $[001]$ and $[110]$ zone axes (ZAs). To this end, projected structures of the different faults are investigated in the fcc and $L1_2$ structures in

both [001] and [110] projection and compared to experimental HRSTEM micrographs acquired in a CoNi-base superalloy and corresponding multislice simulations. The HRSTEM contrast observed at inclined SFs is rationalized by probe intensity distribution simulations.

2 Results and Discussion

The analysis method presented here is based on the fact that an SF in inclined orientation gives rise to additional bright spots in a high-angle annular dark-field (HAADF) HRSTEM micrograph. An example from a relatively thin sample area is shown in Fig. 1c. This micrograph contains both “edges” of the SF where the fault is confined by the foil surfaces as indicated in the schematic side view; in the micrograph these edges are oriented vertically. The atomic columns in both half-crystals on either side of the SF do not align in projection; therefore, a superposition of both lattices is visible where the half-crystals overlap, and the observed shift between them depends on the SF type as will be shown below.

The micrograph at the top right of Fig. 1c shows a magnified view of the region where both lattices are visible. Notably, this region of visible overlap does not extend across the entire projected width of the SF, but it is confined to one of the edges. This is because, as soon as the top half-crystal has reached a sufficient thickness within the foil, the probe can no longer establish a substantial enough channeling condition necessary for atomic-column HAADF contrast [39, 40] in the lower half-crystal. The details of HAADF contrast formation at an inclined SF are elucidated in greater detail in Section 2.4. Consequently, the superposition of both lattices is only visible where the SF is near the top of the foil, making the “top edge” of the SF easily distinguishable from the “bottom edge”. As demonstrated in Fig. 1e, SFs themselves can easily be discerned in ADF-STEM micrographs by the bright band of contrast they produce. This micrograph also shows the single crystalline, two-phase microstructure of the ERBOCo-4 alloy examined in this study, consisting of cuboidal precipitates of the γ' phase with $L1_2$ crystal structure embedded into the fcc γ matrix phase.

In the following, to facilitate a systematic comparison between projected intrinsic and extrinsic fault structures, SF images will be oriented so that the top edge is on the left and the depth of the SF in the foil increases towards the right. First, SFs in the fcc structure are discussed, followed by an analysis of SFs in the ordered $L1_2$ structure.

2.1 Stacking fault analysis in fcc structure

Fig. 2 visualizes the translation vectors and projected structures of ISFs (green) and ESFs (purple) on the inclined (111) plane in the fcc structure for the [110] and [001] ZAs. Due to crystal symmetry, this discussion also applies to other $\langle 110 \rangle$ - and $\langle 001 \rangle$ -type ZAs combined with other inclined $\{111\}$ glide planes, respectively, as long as the fault is oriented so that its top edge is on the left and its depth within the foil increases towards the right. As indicated in the illustration, the angle of the (111) plane to the foil plane differs between the two ZAs (approx. 35.3° for the [110] ZA and 54.7° for the [001] ZA).

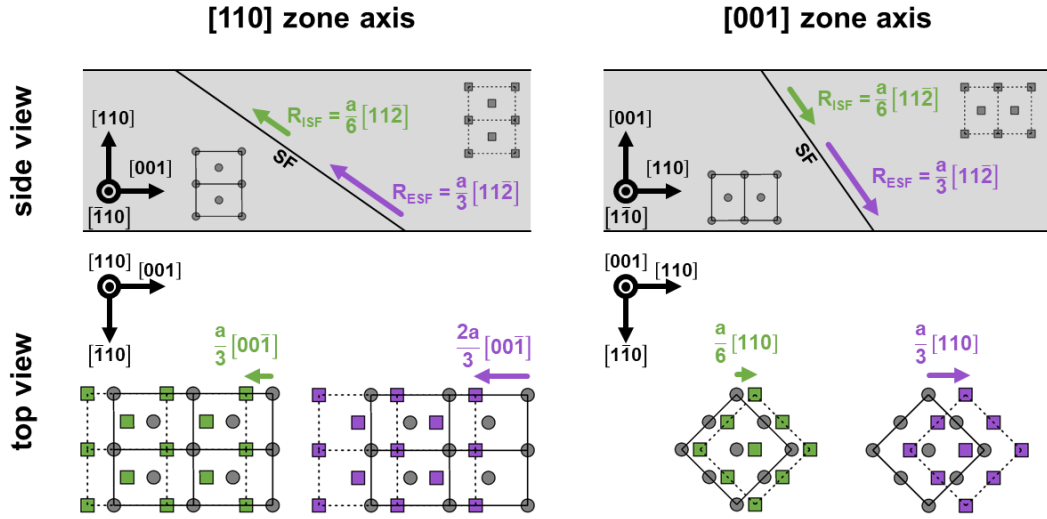


Fig. 2: Schematic overview of inclined SFs and their projected structures in the [110] and [001] ZAs in the fcc crystal structure. The atoms of the reference lattice are represented by circles; those of the shifted lattice are represented by squares. The latter are colored green for ISFs and purple for ESFs in the top-view superposition of both lattices.

In the side view of the foil (see upper part of Fig. 2), the left half crystal will be referred to as the reference lattice (atoms represented by circles, solid unit cell), and the right half crystal as the shifted lattice (atoms represented by squares, dashed unit cell). Therefore, for this analysis, it is more intuitive to describe translations as being applied to the top crystal (contrary to the usual convention for the fringe contrast method where translations are applied to the bottom crystal [41]). The lattice translations R_{ISF} and R_{ESF} introduced by the two fault types are exemplarily shown as arrows. It should be noted that, in each glide plane, the lattice translation required for an ISF can be achieved by three distinct $a/6 \langle 112 \rangle$ -type translation vectors with different directions; the same is true for the $a/3 \langle 112 \rangle$ -type net translation vectors of ESFs.

However, in both cases, they result in identical fault structures; therefore, only one of each is described without loss of generality. A detailed description of translation vectors and their projections [8, 42] can be found in Supplementary Notes 1, 2, and Supplementary Fig. 1-3 in the Supplementary Information (SI).

The projected fault structures, i.e., the superpositions of reference and shifted lattice as observed in the respective ZA, are visualized in the lower part of Fig. 2. In the [110] ZA, the lattice translation introduced by the ISF leads to a projected shift along the [001] direction to the left (towards the fault's top edge) by one third of the lattice periodicity ($\frac{a}{3} [00\bar{1}]$). The atomic columns of the shifted lattice can therefore be described as appearing “to the left” of those of the reference lattice. On the other hand, the ESF lattice translation is twice as large, with a projected shift $\frac{2a}{3} [00\bar{1}]$. Effectively, the atomic columns of the shifted lattice appear “to the right” of those of the reference lattice. (It should be noted that an ESF, which consists of two ISFs on neighboring planes, possesses a central fault plane which is not part of either half crystal. However, as this plane is only a single atom thick, its contribution to HAADF image contrast is negligible; therefore, it is sufficient to consider only the net translation of the ESF here.)

In the [001] ZA, the projected shifts corresponding to R_{ISF} and R_{ESF} appear along the [110] direction; their values are $\frac{a}{6} [110]$ and $\frac{a}{3} [110]$, corresponding to a shift to the right by one third and two thirds of the lattice periodicity, respectively. Thus, for an ISF, columns of the shifted lattice appear “to the right”, whereas for an ESF, they appear “to the left” in this ZA.

Overall, a distinction between ISFs and ESFs is therefore possible in both ZAs, which will be demonstrated by experimental examples as well as simulations in the following.

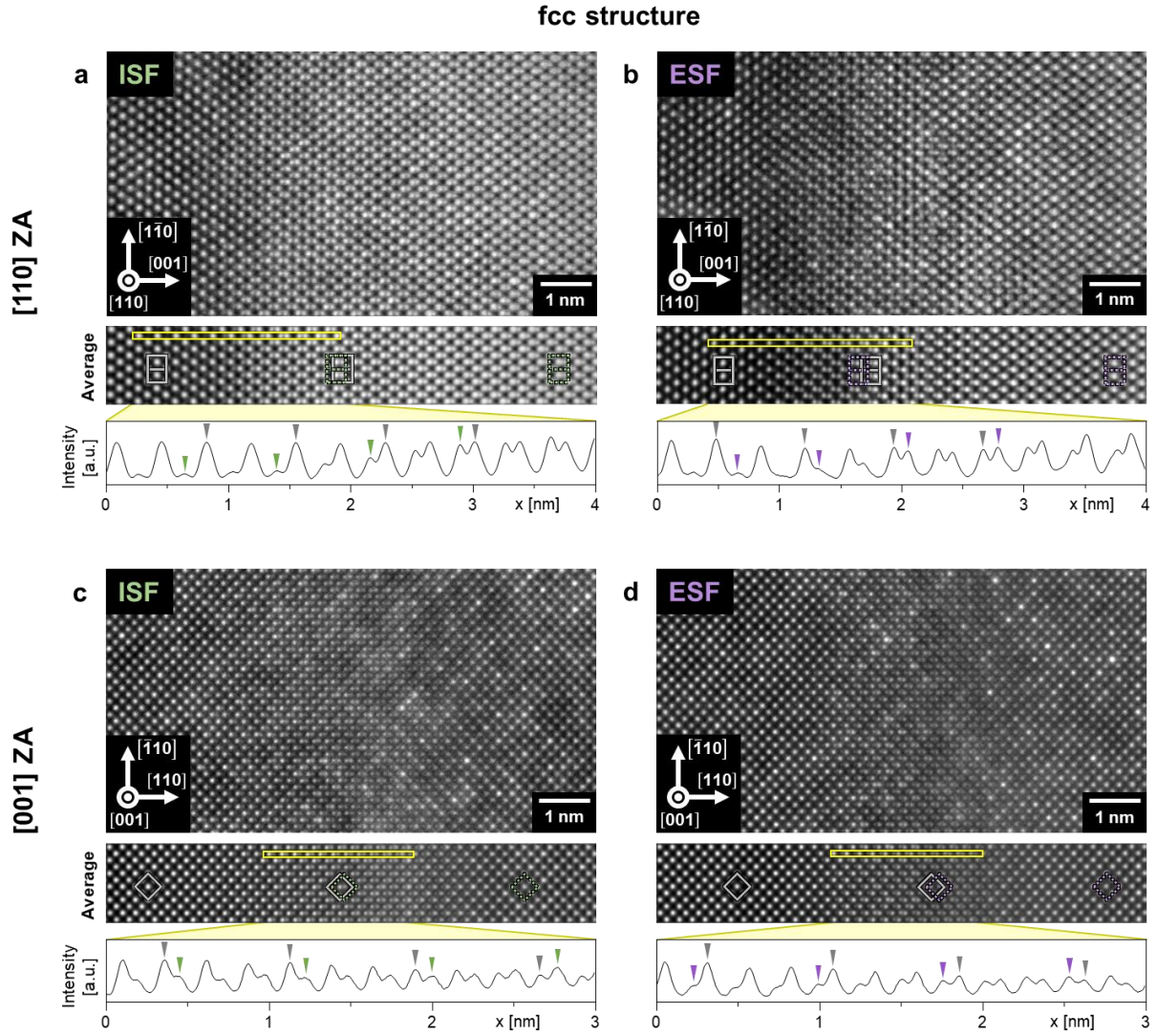


Fig. 3: Experimental HRSTEM micrographs of SFs in the fcc structure. Examples of (a) ISF and (b) ESF in the $[110]$ ZA as well as (c) ISF and (d) ESF in the $[001]$ ZA are shown. Below each micrograph, averages of periodically repeating units are shown along with line scans extracted from the regions marked by yellow rectangles. The positions of unit cells of the reference and shifted lattice are indicated in the averaged images.

Fig. 3a,b presents experimental HRSTEM micrographs in the $[110]$ ZA recorded at the top edges of SFs in fcc γ channels of the microstructure. (Surface roughness of the TEM foil at the atomic scale may lead to the top edge of an SF not appearing as a perfectly straight line at this magnification.) The two cases described above, where a new lattice appears shifted along the $[001]$ direction to the left (Fig. 3a) or right (Fig. 3b) of the reference lattice, can be clearly distinguished. The difference between the two is made even clearer by exploiting the fact that the micrographs consist of periodically repeating units in the vertical direction and averaging these periodic units as shown below the micrographs. (The full micrographs from which the regions shown in Fig. 3 and Fig. 5 were taken are presented in Supplementary Fig. 4 in the SI.).

Intensity line scans measured horizontally across the row of spots marked by yellow rectangles in the averaged experimental data also readily visualize the difference between the appearance of columns of the shifted lattice on the left and on the right side of the reference lattice, respectively, allowing for the distinction between ISF and ESF in this ZA.

Analogously, in the [001] ZA (Fig. 3c,d), the cases where columns of the shifted lattice appear to the right (Fig. 3c) or to the left (Fig. 3d) of the reference lattice are also well distinguishable in experimental micrographs. The experimental data match the expected projected structures described above for ISF and ESF. As atomic columns are more closely spaced along the [110] direction (along which the projected shifts are observed in this ZA), good microscope alignment and precise tilting into ZA orientation are particularly important in this case.

To obtain further confirmation for the correspondence between fault structure and resulting image contrast, HAADF-STEM multislice image simulations were performed for the ISF and ESF fault structures in both ZAs (see Supplementary Fig. 5a in the SI); in all four cases, the resulting images can be clearly matched to their experimental counterparts.

2.2 Stacking fault analysis in $L1_2$ structure

In the $L1_2$ structure, further distinctions between fault types – complex or superlattice SFs – arise from the presence of superlattice ordering (cf. Supplementary Fig. 1 and Supplementary Note 1 in the SI). However, regarding the difference between intrinsic and extrinsic SFs, the analysis of inclined SFs in the $L1_2$ structure is fundamentally very similar to that in the fcc structure as only the stacking sequence, i.e., the position of atomic columns, needs to be considered, as opposed to which columns appear brighter and which appear darker. Typically, superlattice SFs have considerably lower energies than their complex counterparts [29, 42]; thus, extended faults can be assumed to be non-complex. The analysis method presented here is therefore aimed at distinguishing between superlattice intrinsic (SISFs) and superlattice extrinsic stacking faults (SESFs). A discussion for inclined complex SFs and a comparison to superlattice SFs can be found in Supplementary Note 3 and Supplementary Fig. 6 in the SI.

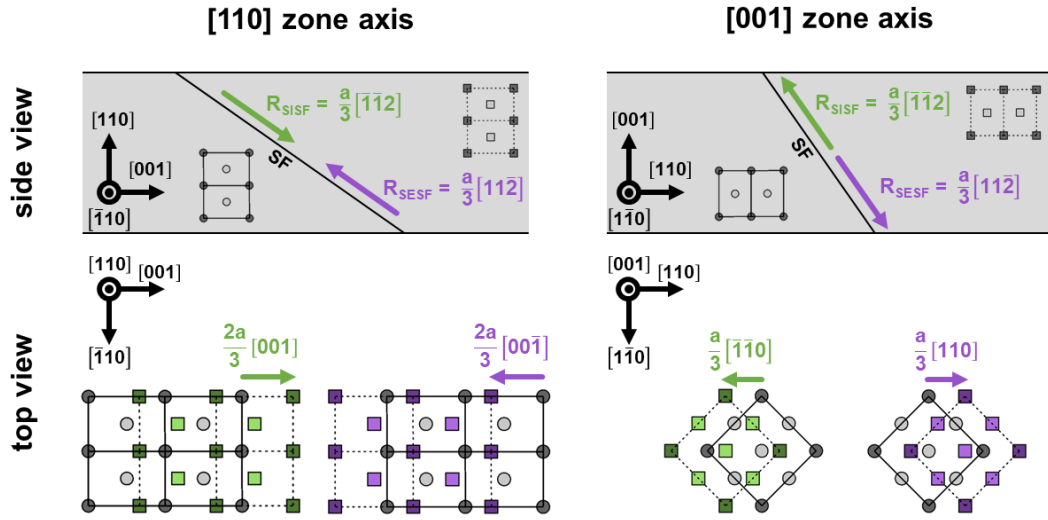


Fig. 4: Schematic overview of inclined SFs and their projected structures in the $[110]$ and $[001]$ ZAs in the L_{12} crystal structure. The atoms of the reference lattice are represented by circles; those of the shifted lattice are represented by squares. The latter are colored green for ISFs and purple for ESFs in the top-view superposition of both lattices. Brighter and darker colors represent the two different sublattices of the ordered structure.

Fig. 4 gives a schematic overview of the translation vectors and projected structures of SISFs and SESFs on the inclined (111) plane for the $[110]$ and $[001]$ ZAs. As above, this discussion is also valid for other inclined $\{111\}$ glide planes viewed in other $\langle 110 \rangle$ - and $\langle 001 \rangle$ -type ZAs, respectively. Again, each fault is oriented so that its top edge is on the left and its depth in the foil increases towards the right.

In Fig. 4, atoms of the reference and shifted lattice are represented again by circles and squares, respectively. To differentiate between the two sublattices of the A_3B -type L_{12} structure, brighter (A) and darker shades (B) of the respective colors are used. As schematically illustrated in the side view, the lattice translation vector associated with a SISF in the L_{12} structure is twice as long as that of an ISF in the fcc structure, and its direction is reversed. Its reversed direction makes the SISF distinguishable from the SESF, whose net translation vector has the same magnitude (see Supplementary Note 1 and Supplementary Fig. 1 in the SI for details). As above, it should be noted that, for each fault type, different translation directions are available; however, they result in identical fault structures, and so only one is shown.

From the visualization of projected fault structures (lower part of Fig. 4), it is evident that inclined SISFs and SESFs can be distinguished in the same way as ISFs and ESFs above: In $[110]$ projection, for the SISF, the shifted lattice is translated to the right (along the $[001]$

direction) by two thirds of the lattice periodicity, its atomic columns therefore appear to the left of the reference lattice, and vice versa for the SESF. In $[001]$ projection, the translation appears along the $[110]$ direction, and the situation is reversed. All four cases are experimentally demonstrated in the following.

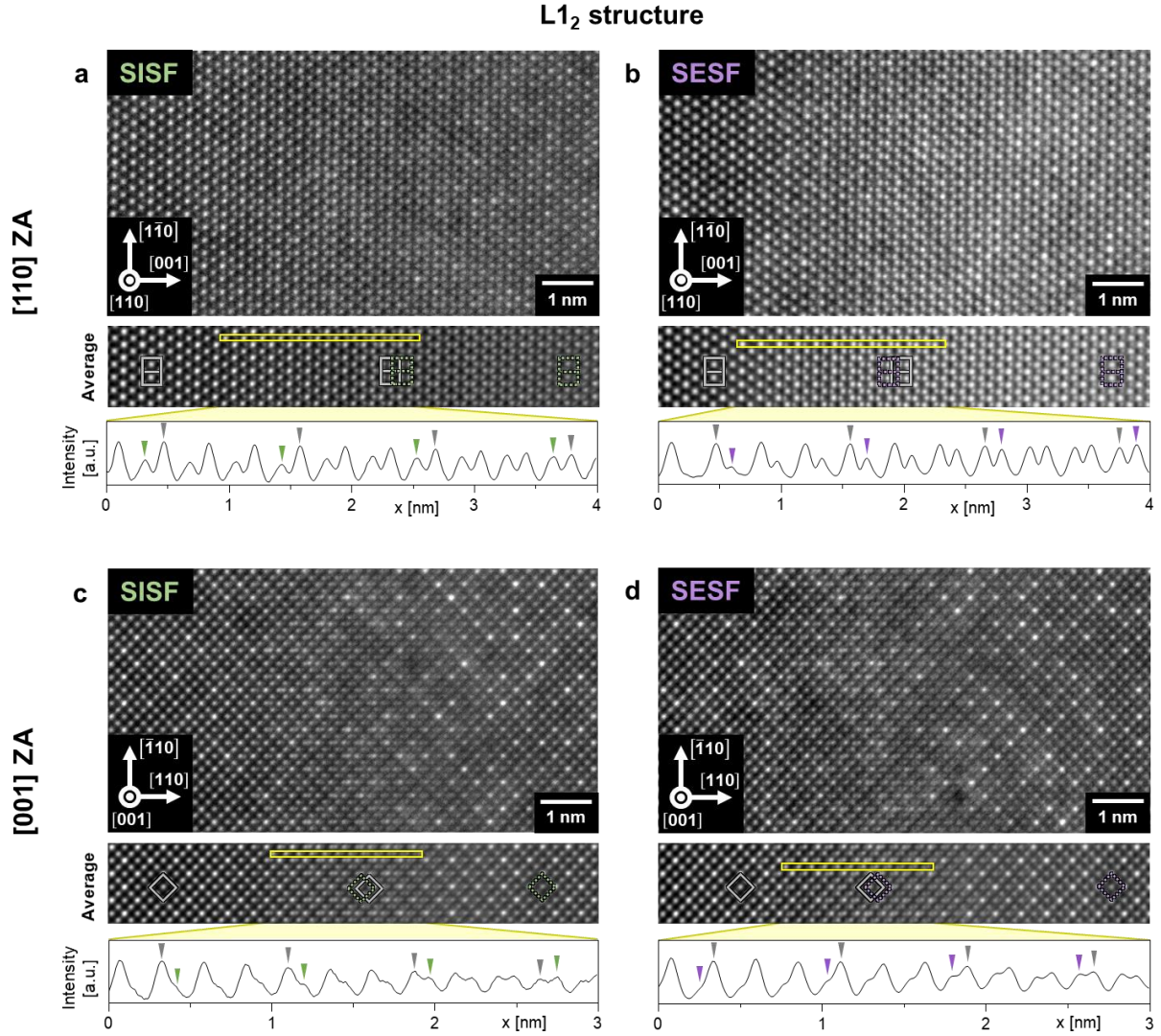


Fig. 5: Experimental HRSTEM micrographs of SFs in the L1₂ structure. Examples of (a) SISF and (b) SESF in the $[110]$ ZA as well as (c) SISF and (d) SESF in the $[001]$ ZA are shown. Below each micrograph, averages of periodically repeating units are shown along with line scans extracted from the regions marked by yellow rectangles. The positions of unit cells of the reference and shifted lattice are indicated in the averaged images.

In the $[110]$ ZA (Fig. 5a,b), the appearance of columns of the shifted lattice to the left (Fig. 5a) or to the right (Fig. 5b) of the reference lattice can be clearly distinguished, revealing that the former is an SISF and the latter an SESF. It should be noted that the superstructure gives rise to two different types of atomic columns in $[110]$ projection: those containing only atoms of

the A sublattice, and mixed columns containing both. Due to the difference in average atomic number between these two types of columns, they exhibit a slight difference in intensity (Z contrast).

The difference between SISF and SESF is also revealed by experiment in [001] projection (Fig. 5c,d) by the appearance of columns of the shifted lattice to the right (Fig. 5c) or to the left (Fig. 5d) of the reference lattice, respectively. Notably, the superstructure is more distinctly visible in the [001] ZA as no mixed-sublattice atomic columns appear in this projection, but rather columns containing only the A sublattice (appearing darker) or only the B sublattice (brighter).

Again, HAADF-STEM multislice image simulations were performed for the fault structures of SISF and SESF in both ZAs (see Supplementary Fig. 5b in the SI), and the simulated images are in good agreement with their experimental counterparts.

In summary, the ability to distinguish between intrinsic and extrinsic SFs in the fcc and $L1_2$ structures has been demonstrated for the [110] as well as [001] ZAs. In the following, practical considerations of this technique are discussed, followed by an investigation of the contrast formation mechanism.

2.3 Practical considerations

HRSTEM-based SF analysis has several advantages over the classical fringe-based methods. It is reliable even at very low thicknesses – and, due to the local nature of HRSTEM contrast, for very short SF segments – where fringe contrast may not be useful. At the same time, the method we have presented is still viable even at a relatively high foil thickness. Two examples – one in the [110] ZA at a thickness of approx. 100 nm and one at a thickness of approx. 130 nm in the [001] ZA – are presented in Supplementary Fig. 7 in the SI. The foil thickness in the respective regions was calculated from the projected thickness of SFs in lower-magnification images as well as the known relationship between fault plane and foil normal [33].

Even at these relatively high foil thicknesses, the HRSTEM contrast can be clearly interpreted with respect to the fault type. TEM sample thicknesses of ~100 nm are routinely achieved by various preparation methods on different material systems, making this SF analysis method easily accessible from a preparation perspective.

Another advantage, especially at higher SF densities, is the ability to analyze SFs which overlap in projection (Fig. 6), as only the contrast near the top edge of the fault is relevant to the analysis. In the example shown in Fig. 6a in the $[110]$ ZA, two inclined SFs near the center of the image are overlapping, which impedes fringe-based analysis as shown in the dark-field TEM image of the same region in the inset. On the other hand, by analyzing the HRSTEM contrast near the top edge of each SF by itself (Fig. 6b,c), both can be identified as extrinsic.

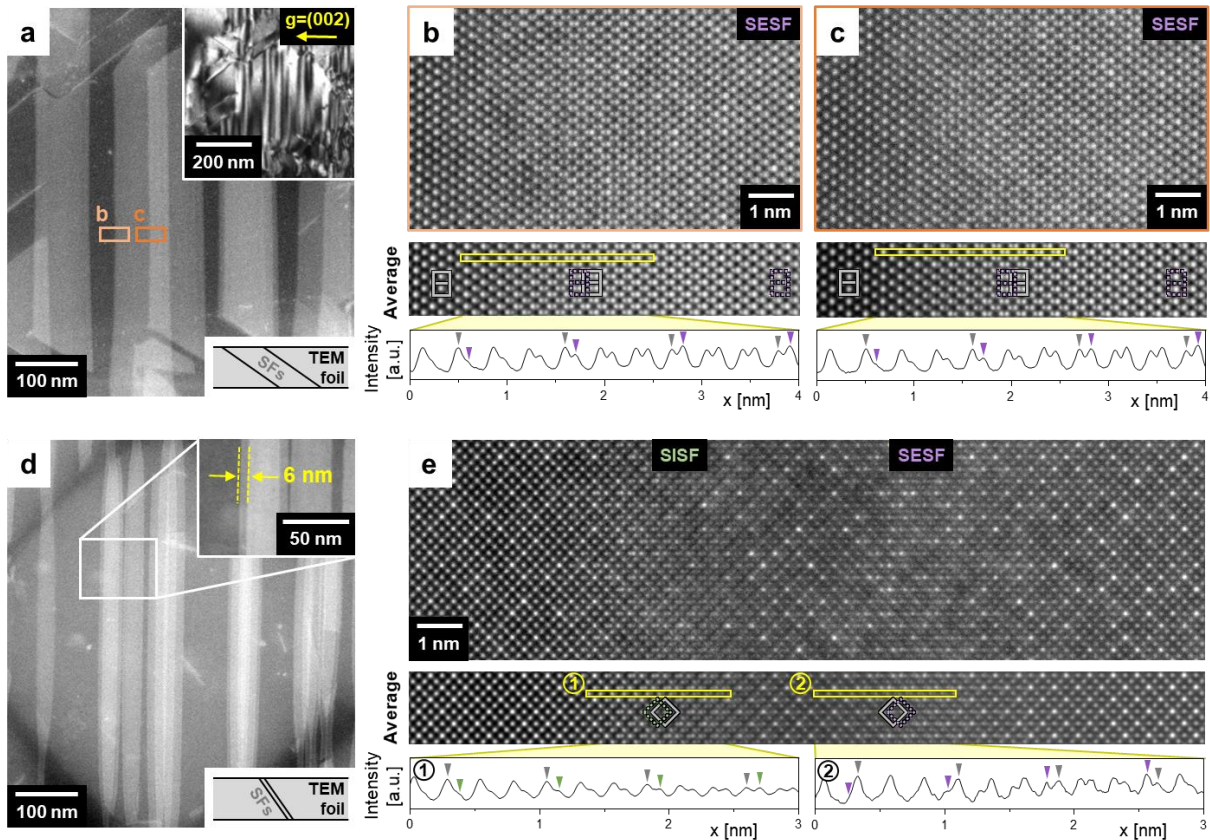


Fig. 6: Analysis of SFs overlapping in projection. (a) ADF-STEM micrograph of overlapping SFs in the $[110]$ ZA. The inset at the top shows a dark-field TEM image of the same region. (b,c) HRSTEM micrographs of the locations marked by rectangles in (a), from which both faults can be identified as extrinsic. (d) ADF-STEM micrograph of closely overlapping SFs in the $[001]$ ZA whose top edges are separated by only 6 nm (see magnified inset). (e) HRSTEM micrograph containing the top edges of both SFs, from which both faults can be characterized. Below each HRSTEM micrograph, the periodically averaged signal is shown along with intensity linescans from the areas marked by yellow rectangles.

A more extreme example of overlapping SFs is shown in Fig. 6d in the $[001]$ ZA. The top edges of the two SFs towards the left side are separated by only 6 nm (see inset). The HRSTEM micrograph in Fig. 6e contains the top edges of both SFs, and even at this small separation, each

SF can be analyzed separately: the fault on the left is intrinsic, whereas the fault on the right is extrinsic.

Generally, the resolution requirement to resolve atomic columns of both lattices in the overlapping region individually is particularly high, as exemplified by the projected distance between the nearest atomic columns of the reference and shifted lattice. In the [110] ZA, this distance equals $a/3$ [001] which, in the case of Ni ($a = 3.52 \text{ \AA}$), corresponds to 117 pm. In the [001] ZA, the projected distance between columns is even smaller at $a/6$ [110], corresponding to 83 pm. To achieve this resolution, careful aberration correction is crucial. However, the method presented in this work requires only the direction of relative shift between both lattices to be detected. The resolution requirement for this distinction is considerably lower, making the application of this method possible even in non-aberration-corrected STEM.

A limitation of the method presented here is that only the net translation vector of a fault can be seen, similar to fringe-based methods. If microtwins or configurations consisting of closely spaced SFs (e.g., [43, 44]) are present in the microstructure, distinguishing between them and intrinsic/extrinsic SFs will be difficult using this method. Only [110]-ZA edge-on fault analysis reveals the exact stacking sequence of planes.

2.4 Contrast formation at inclined faults

To gain a deeper understanding of the contrast formation where reference and shifted lattice overlap in the image, multislice probe propagation simulations have been carried out (Fig. 7).

As a reference, Fig. 7a shows a simulated HAADF-STEM micrograph of an inclined ISF in the fcc structure. Three regions are highlighted: the perfect crystal on the left, the region where the SF is near the top surface and a superposition of reference and shifted lattice is visible in the HAADF-STEM image, and the region to the right where the SF is deeper within the foil and only the shifted lattice is visible in the micrograph. The contrast formation for each of these three situations is discussed in the following.

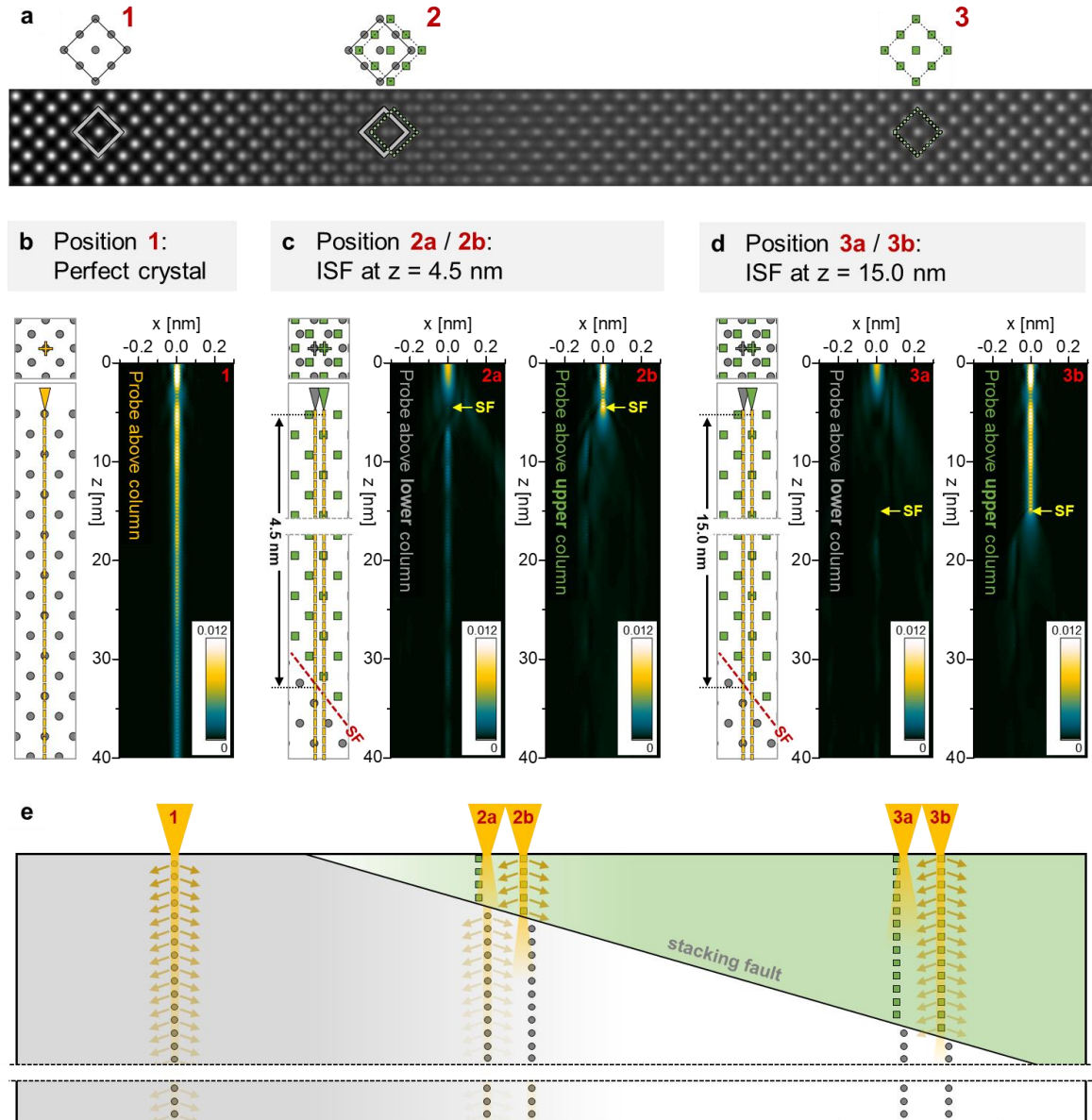


Fig. 7: Simulated probe intensity distributions and HAADF-STEM contrast formation at inclined SFs. (a) HAADF-STEM multislice image simulation of an inclined ISF in fcc Ni in the [001] ZA. Three regions are highlighted: perfect crystal (1), inclined SF near the top surface with visible superposition of reference and shifted lattice (2), and inclined SF at larger depth with only the shifted lattice visible (3). (b-d) Probe propagation simulations in three different structures: (b) perfect fcc crystal, (b) crystal with an inclined ISF at a depth of 4.5 nm, (c) crystal with an inclined ISF at a depth of 15.0 nm. The left side of each subfigure shows a schematic visualization of part of the corresponding crystal in top view (top) and side view (bottom) along with the chosen probe positions. In (b), the probe (yellow) is centered above an atomic column; in (c) and (d), two cases are shown where the probe is centered above a column of the crystal below the SF (grey) and above SF (green), respectively. The plots show a vertical slice of the probe intensity distribution at the location of the incident probe. To enhance the visibility of lower intensities, a non-linear scale is used ($\gamma=0.58$); plots in a linear and a logarithmic scale can be found in Supplementary Fig. 9 in the SI. In all cases, the size of the simulated cell is approx. $5 \times 5 \times 40 \text{ nm}^3$. (e) Schematic side-view illustration of a foil containing an inclined SF, visualizing where channeling of the electron probe (depicted in yellow) occurs, which leads to high-angle scattering (represented by arrows) and a contribution to HAADF signal.

Fig. 7b shows the probe intensity distribution projected along the viewing direction through the simulated cell of a perfect Ni crystal illuminated in the [001] ZA. The probe is centered on an atomic column, as indicated by the yellow cross in the top-view inset at the upper left. A corresponding side view of a portion of the crystal, including the probe position, is shown below. The probe intensity distribution on the right clearly reveals strong channeling of the probe along the atomic column, consistent with the expected behavior in a perfect crystal [45]. Channeling plays a significant role in HAADF contrast formation, as the image intensity primarily arises from electrons scattered out of the strongly channeled probe [46]. Thus, as illustrated on the left side of Fig. 7e, scattering from the probe at the atomic column contributes to the HAADF-STEM image intensity down to a considerable depth within the crystal, although the probe – and consequently the scattering – gradually decreases in intensity with increasing depth.

For the simulations shown in Fig. 7c, an ISF has been introduced into the crystal at a depth of 4.5 nm. In the schematic illustration, the upper, shifted portion of the lattice is represented by green atoms. As indicated in both the top and side views, probe propagation simulations were carried out for two distinct probe positions: one centered above an atomic column in the lower, reference lattice (grey cross), and the other above a column of the upper, shifted lattice (green cross).

When the probe is centered on a column of the lower lattice, it initially traverses the upper portion of the sample in a non-channeling condition, resulting in significant delocalization of its intensity. However, as the residual probe propagates into the lower lattice, it still enters a channeling condition, albeit at reduced intensity. This behavior is illustrated in Fig. 7e and explains why, up to a certain thickness of the upper lattice, atomic columns from the underlying lattice remain visible, leading to the characteristic region of overlapping lattices in HRSTEM micrographs.

On the other hand, when the probe is centered on a column of the upper lattice, strong channeling occurs until the probe encounters the lower lattice, where the channeling condition is disrupted. As a result, only the region above the stacking fault contributes significantly to the HAADF atomic-column contrast, while the region below contributes minimally. This is illustrated in Fig. 7e and explains why atomic columns of the upper lattice remain clearly visible in micrographs, even when these columns are relatively short.

Finally, in Fig. 7d, the ISF is positioned deeper within the crystal, at a depth of 15.0 nm. As before, probe propagation simulations were performed with the probe placed above an atomic column in the lower lattice (grey cross) and in the upper, shifted lattice (green cross).

When the probe is now placed above a column of the lower lattice, it remains in a non-channeling condition over a longer distance compared to the previous case, leading to much greater delocalization of its intensity. By the time the SF is reached, virtually no probe intensity remains to establish a channeling condition. Consequently, there is no significant scattering of electrons to large angles from this column, and the lower lattice does not produce observable HAADF contrast.

In contrast, a probe centered on a column of the upper lattice immediately enters a channeling condition, which it maintains over a long propagation distance until it reaches the lower lattice where it becomes dechanneled. Thus, atomic-column HAADF contrast is generated from the upper crystal.

In summary, going from left to right in Fig. 7a and e, as the SF appears and its depth increases, the atomic columns of the shifted lattice become longer, allowing the probe to maintain channeling along them over a greater distance. This leads to an increasing HAADF contrast contribution from the upper, shifted lattice. Simultaneously, channeling at the atomic columns of the lower, reference lattice progressively diminishes as the probe undergoes increasing dechanneling within the upper crystal before reaching these columns, thereby reducing their contribution to the HAADF contrast. In this way, a region of overlapping contrast from both lattices emerges in the HAADF signal only when the SF is near the top surface.

2.5 “Quasi-ultrathin” foil effect

A striking feature of HRSTEM micrographs of inclined SFs is the distinct increase in contrast variation between atomic columns to the right of the fault's top edge. It is visible both as a random distribution of brighter columns in the fcc structure (Fig. 3) as well as the increased visibility of the superlattice ordering in the $L1_2$ structure (Fig. 5). The effect still appears at high foil thickness (cf. Supplementary Fig. 7 in the SI) where columns in the perfect crystal exhibit significantly less distinct superlattice contrast.

This effect can be understood by the mechanism of contrast formation described in the above section. If channeling is interrupted after a short distance, the difference in Z-contrast between

atomic columns in the upper crystal is enhanced: the cross-talk between neighboring columns, which increases with increasing thickness [47] and tends to average out intensity differences between those columns, is minimized. Effectively, a “quasi-ultrathin” foil effect emerges, in which the HAADF contrast from the region of the foil where the SF is near the top surface resembles that of a foil only a few nanometers thick. This effect is investigated exemplarily in Fig. 8 for both the fcc and the $L1_2$ structure at a foil thickness of approx. 60 nm.

In the fcc structure, the described effect makes the random distribution of high-Z atoms in the solid solution clearly visible (Fig. 8a). To quantify the change in contrast, the sum intensity of each atomic column in the image was calculated. Columns were then grouped by (220) planes (see inset); within each such plane, as a measure of contrast variation, the coefficient of variation (CV), i.e., the standard deviation of the atomic column intensities for a given plane normalized by their mean intensity, was determined. These CV values for each plane are plotted below the micrograph in Fig. 8a against the depth of the SF in the foil at that plane (as calculated from the crystallographically defined angle between fault plane and ZA [33]). The gray-shaded area marks the sample region with overlapping contrast between the reference and shifted lattices, which has been excluded from the analysis. The horizontal line drawn in the plot represents the baseline CV obtained from (220) planes in the perfect crystal to the left of the SF. Where the SF is near the top of the foil, an increase in intensity variation by up to 99 % is clearly revealed.

The schematic side-view illustration above the micrograph visualizes the different sample regions present in the imaged area: perfect crystal without SF (1), region of visible overlap between reference and shifted lattice (2), “quasi-ultrathin” region with inclined SF at low depth, where only the part above the SF (hatched area) is visible with enhanced Z-contrast (3), and region with inclined SF at larger depth (4).

At a different location within the “quasi-ultrathin” region along the SF, still within the γ phase, enhanced Z-contrast reveals a cluster exhibiting superlattice ordering. The corresponding HRSTEM image and CV analysis are shown in Supplementary Fig. 10 in the SI. The image clearly identifies the cluster as a nano-precipitate of the γ' phase, leading to alternating high and low CV values of (220) planes. It is likely a tertiary γ' precipitate that formed during cooling from creep temperature, as a result of oversaturation of γ' -forming elements in the γ matrix. Without the “quasi-ultrathin” foil effect, this phenomenon would likely remain undetected.

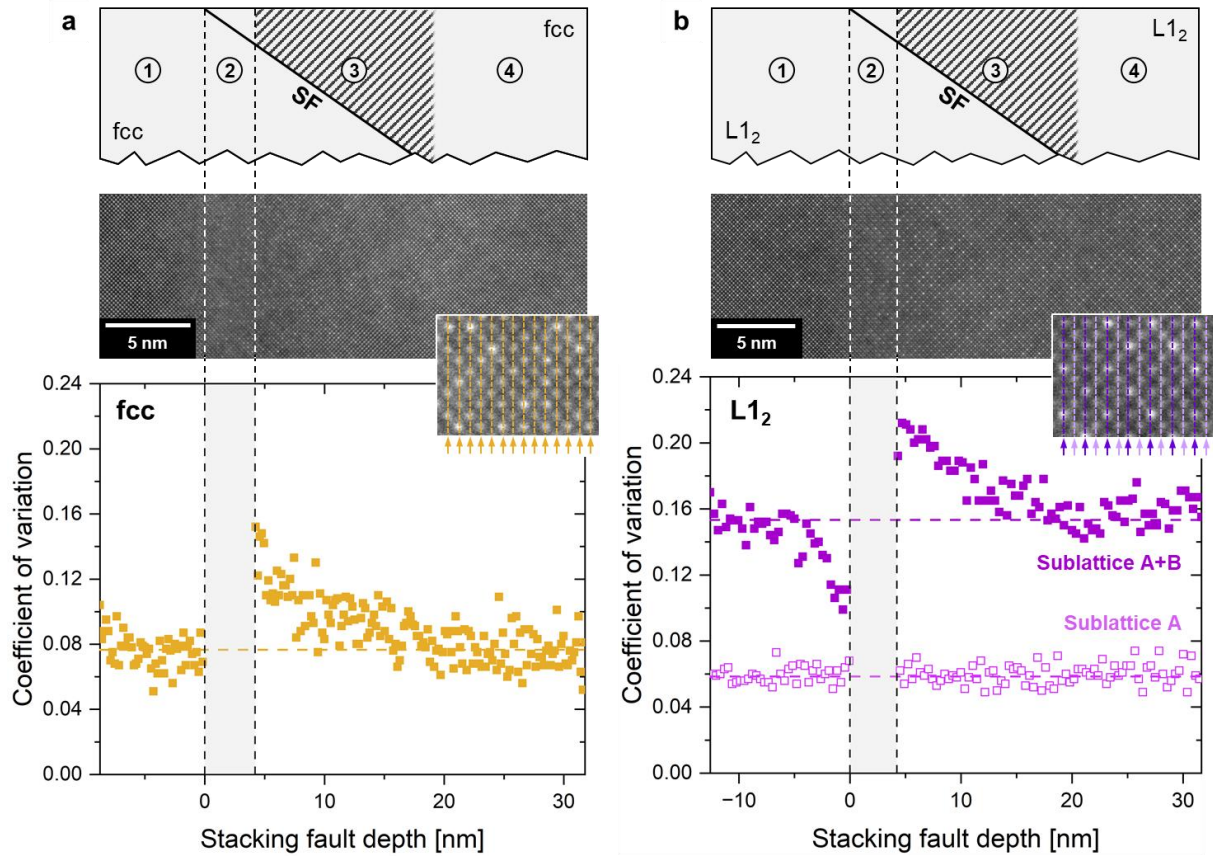


Fig. 8: Analysis of enhanced Z-contrast above inclined SFs. (a) HRSTEM micrograph of an inclined SF in the fcc structure. The plot below shows the CV of atomic-column intensities within each (220) plane (see inset). The horizontal line represents the baseline CV determined in a region of perfect lattice to the left of the SF. (b) Analogous evaluation of an inclined SF in the L1₂ structure. For this plot, (220) planes containing columns of only one sublattice and those containing both sublattices (see inset) were considered separately. The HRSTEM images shown in (a,b) were stitched together from two separate micrographs, respectively, to obtain a field of view containing regions to the left and right of inclined SFs. Above each micrograph, a schematic side-view illustration visualizes the region of perfect crystal (1), region of visible overlap between reference and shifted lattice (2), "quasi-ultrathin" region with inclined SF at low depth (3), and region with inclined SF at larger depth (4). The hatched area (3) represents the sample region contributing to the enhanced Z-contrast. The full HRSTEM images on which the analysis was performed can be found in Supplementary Fig. 11 in the SI.

Contrast variations near an SF in the L1₂ structure have been evaluated (Fig. 8b) in the same way as for the fcc structure. Due to the superlattice ordering in this structure, two different types of (220) planes appear alternately, as highlighted in the inset: those containing only columns of the A sublattice (arrows and dashed lines in lighter color) and those containing alternating columns of the A and B sublattice (darker color). For the plot, both types of planes were considered separately. It is evident that contrast variations in the planes containing only the A sublattice remain negligible across all SF depths. This is related to the similar atomic numbers of Co and Ni, which occupy the A sublattice in the CoNi-base superalloy ERBOCo-4. In

contrast, the CV of the mixed planes increases significantly by up to 38 % at low SF depths. This is attributed to the reduced cross-talk of the electron probe between neighboring atomic columns, which enhances the contrast between low-Z (Al/Cr/Ti) and high-Z (Ta/W) elements on the B sublattice. Additionally, due to the systematic variations in intensity of the two different sublattices, the baseline of the CV is significantly higher than for the A sublattice and the fcc structure.

These brief examples show that the contrast observed at inclined SFs provides opportunities for analysis even beyond characterization of the SF itself: the possibility to investigate atomic-column contrast from a region only a few nm thick without requiring an extremely thin foil may prove useful for future high-resolution studies, e.g., of short-range ordering, site occupancy, or clustering phenomena. Similar, and in fact even more pronounced, de-channeling effects than those observed for inclined SFs are expected to occur at grain boundaries or phase boundaries located at shallow depths beneath the surface of the TEM lamella. We therefore propose that other two-dimensional defects should also be considered in the context of the “quasi-ultrathin” foil effect.

4 Summary and conclusion

Our novel approach to stacking fault (SF) analysis using high-resolution scanning transmission electron microscopy (HRSTEM) of inclined faults overcomes the long-standing limitations of the two classical SF analysis methods that have been employed for decades. The new method is highly flexible and robust in determining the intrinsic or extrinsic character of stacking faults, as demonstrated in both the fcc and $L1_2$ crystal structures of a compression-deformed superalloy. It is applicable to both $[110]$ and $[001]$ zone axis projections and relies on evaluating the relative displacement between the projected crystal lattices above and below the stacking fault. These lattices appear directly superimposed in HAADF-HRSTEM micrographs near the intersection of the stacking fault with the upper surface of the TEM lamella. We showed that the method remains applicable even at foil thicknesses typical for conventional TEM (> 100 nm) and in cases where SFs significantly overlap in projection, as only the contrast formed near the top edge of the SF is relevant for the analysis. Multislice probe-propagation simulations provided deeper insight into how the SF-induced shifts of atomic columns within the foil influence contrast formation in HRSTEM lattice images. Most importantly, when combined with the well-established HRSTEM analysis of edge-on SFs, the proposed method enables, for

the first time, reliable analysis of SFs on all four {111} glide planes in a single sample using one microscopy technique. Although demonstrated for SFs in fcc and L1₂, the underlying principle is transferable to other crystal structures as well and is expected to facilitate defect characterization across a wide range of material systems, including high- and medium entropy alloys, steels, and thin-film systems.

Furthermore, we have shown that the HAADF contrast from the region where the inclined SF approaches the top of the foil closely resembles that of an ultrathin lamella, enabling studies which would traditionally require a very low foil thickness of only a few nanometers. We anticipate that this “quasi-ultrathin” foil effect will have significant practical relevance, for example in studies of long-range ordering, compositional fluctuations, and nanoclustering. We propose extending this concept to other two-dimensional defects, such as grain boundaries or phase boundaries, where de-channeling effects are expected to be even more pronounced than in the case of SFs.

Materials and Methods

Alloy preparation

For the experimental investigation of the inclined SFs, the single-crystalline CoNi-base superalloy ERBOCo-4 (composition in at.%: Co_{43.2}Ni₃₂Al₈W_{5.7}Ti_{2.8}Ta_{1.8}Cr₆Si_{0.4}Hf_{0.1}) [48] was cast using the Bridgman process. To obtain the γ/γ' microstructure, a three-step heat treatment (8 h at 1280 °C, 5 h at 1050 °C, 16 h at 900 °C) was performed. Specimens for compression testing with a diameter of 3 mm and a height of 4.5 mm were fabricated by wire electrical discharge machining. Constant strain-rate compression testing at strain rates of 10⁻³ and 10⁻⁵ s⁻¹ along the [001] direction was performed at an *Instron 4505* electromechanical universal testing machine at a temperature of 850 °C up to a plastic strain of 1 %. [001] and [110] sections were cut from the specimens and ground down to a thickness of 100-150 μ m. To attain electron transparency, samples were electrolytically thinned in a solution of 16.7 % nitric acid and 83.3 % methanol in a *Struers Double Jet Tenupol-5* preparation system at 40 to 45 V and a temperature of -25 °C. Additional details about the alloy fabrication, deformation, and TEM sample preparation can be found in an earlier publication [26].

Transmission electron microscopy

HRSTEM imaging was performed using a probe-corrected *Thermo Fisher Scientific Spectra 200 C-FEG* at 200 kV using the high-angle annular dark field (HAADF) detector and a semi-convergence angle of 30 mrad. For the camera length, values between 62 mm and 198 mm were used, corresponding to collection angle ranges ranging from 90-200 mrad to 28-169 mrad, i.e., HAADF or annular dark-field (ADF) imaging conditions. Where necessary, the influence of scan noise and drift distortions was minimized by recording multiple frames and averaging them. Furthermore, dark-field TEM imaging in a two-beam condition was performed using a *Philips CM 30* TEM at 300 kV.

Crystal files and multislice simulations

The *CrystalMaker X* software (version 10.8.2; CrystalMaker Software Ltd, Oxford) was utilized to generate crystal structures for illustration and image simulation purposes. The multislice simulations for the fcc structure were performed using a pure Ni crystal as a typical representative of this crystal structure, similar in atomic number to the experimentally investigated CoNi-based solid solution. For L1₂, the model Co₃(Al,W) structure was used with a randomized occupation of the B sublattice. This represents the experimentally observed ordered structure well, which also exhibits a higher average atomic number of the B sublattice (i.e., the corners of the unit cell cube). It should be noted that there are also phases in which the A sublattice shows a higher average atomic number, such as the Ni₃Al phase. In such cases, the pattern of brighter and darker atomic columns in HAADF contrast will be inverted.

Multislice simulations of STEM images as well as probe propagation were carried out using the *Dr.Probe* software [49] at an accelerating voltage of 200 kV, a convergence semiangle of 30 mrad, and with no aberrations. HAADF image simulations were performed with an angular detection range of 90-200 mrad, a pixel size of 10 pm, and an effective source size of 0.025 nm.

Determination of intensity variation

Code for the evaluation of atomic-column contrast was written in Python as a Jupiter Notebook [50] using the Hyperspy and Atomap packages [51, 52]. To quantify the increased contrast close to the intersection between the inclined SF and the top of the foil, the integrated intensity of

each atomic column was calculated and its position within the micrograph was determined. Subsequently, atomic columns were grouped according to their distance perpendicular to the intersection of the inclined SF and the top of the foil, i.e., along (220) planes (the vertical planes highlighted by arrows and dashed lines in the inset of Fig. 8). Subsequently, the mean μ and standard deviation σ of each group were calculated and the coefficient of variation (CV) was determined by $CV = \sigma/\mu$. Code generation was assisted by the ChatGPT software (models 4o and o3-mini-high; OpenAI, San Francisco, United States). The analyzed micrographs were manually stitched using CorelDRAW Graphics Suite 2021 (Alludo, Ottawa, Canada) to cover a sufficiently large area such that the increased CVs returned to baseline levels to the left and right of the inclined SF.

Authorship contribution statement

E.S. conceived the research. E.S. and N.K. developed the methodology. N.K. performed TEM experiments and analyzed the data, with contributions from L.M. L.M. and N.K. performed multislice simulations. A.B. performed the analysis of intensity variations. A.B. and S.N. provided specimens of the investigated alloy. N.K. wrote the initial version of the manuscript. E.S. revised the manuscript. All authors contributed to the final version of the manuscript.

Data availability

The raw data pertaining to this study will be made available at Zenodo.

Acknowledgements

The authors gratefully acknowledge funding from the German Research Foundation (DFG) through projects A7 (N.K. and E.S.) and B3 (A.B. and S.N.) of the collaborative research project SFB/Transregio 103 “From Atoms to Turbine Blades - a Scientific Approach for Developing the Next Generation of Single Crystal Superalloys”. A.B. acknowledges financial support from the Alexander-von-Humboldt Foundation.

References

1. Edwards, O.S. & Lipson, H.S. Imperfections in the structure of cobalt. I. Experimental work and proposed structure. *Proceedings of the Royal Society of London Series A Mathematical and Physical Sciences* **180**, 268-277 (1942).
2. Christian, J.W. & Vitek, V. Dislocations and stacking faults. *Reports on Progress in Physics* **33**, 307-411 (1970).
3. Smallman, R.E. & Westmacott, K.H. Stacking faults in face-centred cubic metals and alloys. *Philos Mag* **2**, 669-683 (1957).
4. Trigunayat, G.C. & Verma, A.R. Polytypism and Stacking Faults in Crystals with Layer Structure. In: *Crystallography and Crystal Chemistry of Materials with Layered Structures* (1976).
5. Böer, K.W. & Pohl, U.W. Crystal Defects. In: *Semiconductor Physics* (2023).
6. Su, R., *et al.* The influence of stacking faults on mechanical behavior of advanced materials. *Materials Science and Engineering: A* **803**, 140696 (2021).
7. Camassel, J. & Juillaguet, S. Optical properties of as-grown and process-induced stacking faults in 4H-SiC. *physica status solidi (b)* **245**, 1337-1355 (2008).
8. Hull, D. & Bacon, D.J. *Introduction to Dislocations*, 5 edn. Elsevier (2011).
9. Soleimani, M., Kalhor, A. & Mirzadeh, H. Transformation-induced plasticity (TRIP) in advanced steels: A review. *Materials Science and Engineering: A* **795**, 140023 (2020).
10. Christian, J.W. & Mahajan, S. Deformation twinning. *Prog Mater Sci* **39**, 1-157 (1995).
11. Jian, W.W., *et al.* Physics and model of strengthening by parallel stacking faults. *Appl Phys Lett* **103**, 133108 (2013).
12. Frank, M., *et al.* Direct evidence of the stacking fault-mediated strain hardening phenomenon. *Appl Phys Lett* **119**, 081906 (2021).
13. Suzuki, H. Segregation of Solute Atoms to Stacking Faults. *Journal of the Physical Society of Japan* **17**, 322-325 (1962).

14. Viswanathan, G.B., *et al.* Segregation at stacking faults within the gamma ' phase of two Ni-base superalloys following intermediate temperature creep. *Scripta Mater* **94**, 5-8 (2015).
15. Rae, C.M.F., Matan, N. & Reed, R.C. The role of stacking fault shear in the primary creep of [001]-oriented single crystal superalloys at 750 degrees C and 750 MPa. *Mat Sci Eng a-Struct* **300**, 125-134 (2001).
16. Knowles, D.M. & Chen, Q.Z. Superlattice stacking fault formation and twinning during creep in γ/γ' single crystal superalloy CMSX-4. *Materials Science and Engineering: A* **340**, 88-102 (2003).
17. Viswanathan, G.B., *et al.* Investigation of creep deformation mechanisms at intermediate temperatures in René 88 DT. *Acta Mater* **53**, 3041-3057 (2005).
18. Kovarik, L., *et al.* Microtwinning and other shearing mechanisms at intermediate temperatures in Ni-based superalloys. *Prog Mater Sci* **54**, 839-873 (2009).
19. Vorontsov, V.A., Kovarik, L., Mills, M.J. & Rae, C.M.F. High-resolution electron microscopy of dislocation ribbons in a CMSX-4 superalloy single crystal. *Acta Mater* **60**, 4866-4878 (2012).
20. Titus, M.S., Eggeler, Y.M., Suzuki, A. & Pollock, T.M. Creep-induced planar defects in L1(2)-containing Co- and CoNi-base single-crystal superalloys. *Acta Mater* **82**, 530-539 (2015).
21. Eggeler, Y.M., *et al.* Planar defect formation in the gamma' phase during high temperature creep in single crystal CoNi-base superalloys. *Acta Mater* **113**, 335-349 (2016).
22. Smith, T.M., Rao, Y., Wang, Y., Ghazisaeidi, M. & Mills, M.J. Diffusion processes during creep at intermediate temperatures in a Ni-based superalloy. *Acta Mater* **141**, 261-272 (2017).
23. Lenz, M., *et al.* Tension/Compression asymmetry of a creep deformed single crystal Co-base superalloy. *Acta Mater* **166**, 597-610 (2019).
24. Volz, N., *et al.* Creep properties and deformation mechanisms of single-crystalline gamma '-strengthened superalloys in dependence of the Co/Ni ratio. *Philos Mag* **102**, 718-744 (2021).

25. Bezold, A. & Neumeier, S. Tailoring deformation mechanisms in polycrystalline CoNi-base superalloys for enhanced high temperature strength. *Scripta Mater* **226**, 115250 (2023).
26. Vollhüter, J., *et al.* Strain Rate-Dependent Anomalous Work Hardening of a Single-Crystalline CoNi-Base Superalloy. *Metallurgical and Materials Transactions A* **54**, 1608-1619 (2023).
27. Suzuki, A., Inui, H. & Pollock, T.M. L1(2)-Strengthened Cobalt-Base Superalloys. *Annu Rev Mater Res* **45**, 345-368 (2015).
28. Reed, R.C. *The Superalloys: Fundamentals and Applications*. Cambridge University Press (2006).
29. Eggeler, Y.M., Vamsi, K.V. & Pollock, T.M. Precipitate Shearing, Fault Energies, and Solute Segregation to Planar Faults in Ni-, CoNi-, and Co-Base Superalloys. *Annual Review of Materials Research, Vol 51, 2021* **51**, 209-240 (2021).
30. Pyczak, F., *et al.* Plastic deformation mechanisms in a crept L12 hardened Co-base superalloy. *Materials Science and Engineering: A* **571**, 13-18 (2013).
31. Lenz, M., Wu, M. & Spiecker, E. Segregation-assisted climb of Frank partial dislocations: An alternative route to superintrinsic stacking faults in L12-hardened superalloys. *Acta Mater* **191**, 270-279 (2020).
32. Smith, T.M., Unocic, R.R., Deutchman, H. & Mills, M.J. Creep deformation mechanism mapping in nickel base disk superalloys. *Materials at High Temperatures* **33**, 372-383 (2016).
33. Bezold, A., *et al.* Quantification of the temperature-dependent evolution of defect structures in a CoNi-base superalloy. *Acta Mater* **227**, (2022).
34. Art, A., Gevers, R. & Amelinckx, S. The Determination of the Type of Stacking Faults in Face Centered Cubic Alloys by Means of Contrast Effects in the Electron Microscope. *physica status solidi (b)* **3**, 697-711 (1963).
35. van Landuyt, J., Gevers, R. & Amelinckx, S. On the determination of the nature of stacking faults in F.C.C. metals from the bright field image. *physica status solidi (b)* **18**, 167-172 (1966).
36. Gevers, R., Art, A. & Amelinckx, S. Electron Microscopic Images of Single and Intersecting Stacking Faults in Thick Foils. Part I: Single Faults. *physica status solidi (b)* **3**, 1563-1593 (1963).

37. Sarosi, P.M., Viswanathan, G.B. & Mills, M.J. Direct observation of an extended complex stacking fault in the gamma' phase of a Ni-base superalloy. *Scripta Mater* **55**, 727-730 (2006).
38. Karpstein, N., *et al.* Reliable identification of the complex or superlattice nature of intrinsic and extrinsic stacking faults in the L12 phase by high-resolution imaging. *Acta Mater* **260**, 119284 (2023).
39. Pennycook, S.J. & Jesson, D.E. High-resolution Z-contrast imaging of crystals. *Ultramicroscopy* **37**, 14-38 (1991).
40. Hillyard, S., Loane, R.F. & Silcox, J. Annular dark-field imaging: Resolution and thickness effects. *Ultramicroscopy* **49**, 14-25 (1993).
41. Hashimoto, H., Howie, A. & Whelan, M.J. Anomalous electron absorption effects in metal foils: theory and comparison with experiment. *Proceedings of the Royal Society of London Series A Mathematical and Physical Sciences* **269**, 80-103 (1962).
42. Voskoboinikov, R.E. Effective gamma-surfaces in {111} plane in FCC Ni and L1(2) Ni3Al intermetallic compound. *Phys Met Metallogr+* **114**, 545-552 (2013).
43. Smith, T.M., *et al.* Segregation and Phase Transformations Along Superlattice Intrinsic Stacking Faults in Ni-Based Superalloys. *Metall Mater Trans A* **49a**, 4186-4198 (2018).
44. Bezold, A., *et al.* Recovery of superlattice stacking faults at high temperatures. *Scripta Mater* **222**, 115005 (2023).
45. Howie, A. Diffraction channelling of fast electrons and positrons in crystals. *Philos Mag* **14**, 223-237 (1966).
46. Loane, R.F., Xu, P. & Silcox, J. Incoherent imaging of zone axis crystals with ADF STEM. *Ultramicroscopy* **40**, 121-138 (1992).
47. Dwyer, C. & Etheridge, J. Scattering of Å-scale electron probes in silicon. *Ultramicroscopy* **96**, 343-360 (2003).
48. Volz, N., *et al.* Thermophysical and Mechanical Properties of Advanced Single Crystalline Co-base Superalloys. *Metall Mater Trans A* **49a**, 4099-4109 (2018).
49. Barthel, J. Dr. Probe: A software for high-resolution STEM image simulation. *Ultramicroscopy* **193**, 1-11 (2018).

50. Granger, B.E. & Perez, F. Jupyter: Thinking and Storytelling With Code and Data. *Computing in Science & Engineering* **23**, 7-14 (2021).
51. de la Peña, F., *et al.* hyperspy/hyperspy.). v1.7.3, Oct 2022 edn. Zenodo (2022).
52. Nord, M., Vullum, P.E., MacLaren, I., Tybell, T. & Holmestad, R. Atomap: a new software tool for the automated analysis of atomic resolution images using two-dimensional Gaussian fitting. *Advanced Structural and Chemical Imaging* **3**, 9 (2017).

Supplementary Information

A new angle on stacking faults: Breaking the edge-on limit in high-resolution defect analysis

**Nicolas Karpstein ^a, Lukas Müller ^a, Andreas Bezold ^{b,c},
Steffen Neumeier ^b, Erdmann Spiecker ^{a,*}**

^a Friedrich-Alexander-Universität Erlangen-Nürnberg, Department of Materials Science & Engineering, Institute of Micro- and Nanostructure Research, and Center for Nanoanalysis and Electron Microscopy (CENEM), IZNF, Erlangen, Germany

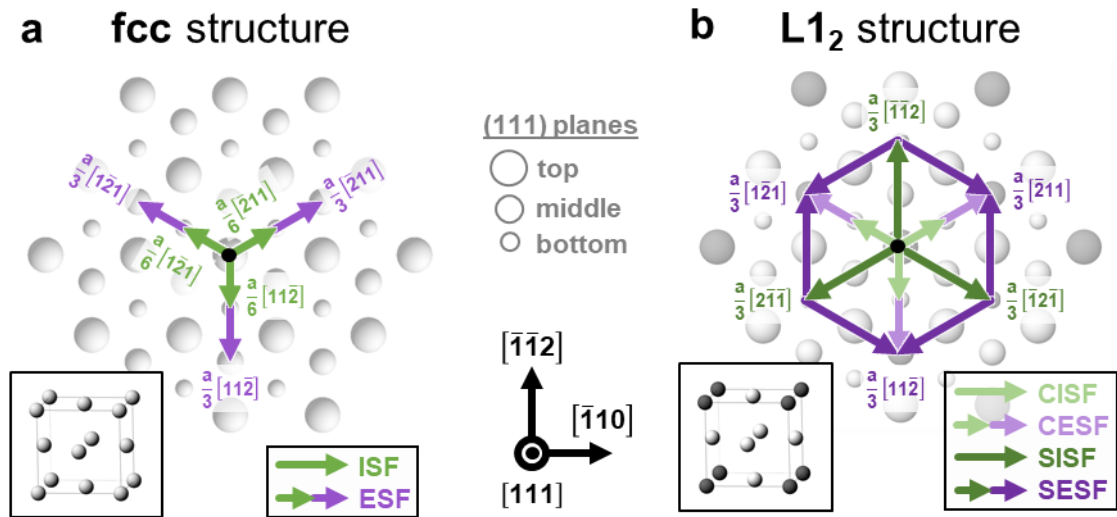
^b Friedrich-Alexander-Universität Erlangen-Nürnberg, Department of Materials Science & Engineering, Institute I: General Materials Properties, Erlangen, Germany

^c The Ohio State University, Department of Materials Science & Engineering, Columbus, OH, USA

Corresponding author: erdmann.spiecker@fau.de

Supplementary Note 1: Stacking fault types and corresponding lattice translations in the fcc and L1₂ crystal structures.

The fcc and L1₂ crystal structures give rise to various SF types, which will be outlined in the following (Supplementary Fig. 1). To visualize the lattice translation associated with each type of stacking fault exemplarily in the (111) glide plane, a stack of three (111) planes is shown where the bottom, middle, and top layer are represented by small, medium-sized and large atoms, respectively. Arrows represent the translation of the top layer against the lower ones required to form a given fault.



Supplementary Fig. 1: Schematic illustration of a stack of three (111) planes in the (a) fcc and (b) L1₂ structures. Unit cells are shown as an inset. The vectors by which the top half-crystal is translated to form a given fault are represented by arrows colored depending on the fault type.

In the fcc structure (Supplementary Fig. 1a), $\frac{a}{6}\langle 211 \rangle$ Shockley partial dislocations introduce intrinsic SFs (ISFs) into the crystal structure (green arrows) and make it appear as though a plane is missing from the ...ABCABC... stacking sequence of close-packed planes. As evident from the illustration, the corresponding translation can occur in three different directions; however, all three translation vectors result in crystallographically identical fault structures. In other words, the difference vector between any two of these vectors is equal to a lattice translation vector. An extrinsic SF (ESF) consists of two ISFs on neighboring glide planes, resulting in net translations of type $\frac{a}{3}\langle 211 \rangle$ as illustrated by purple arrows. In this case, the stacking sequence appears to have an extra plane inserted into it. For simplicity, the arrows

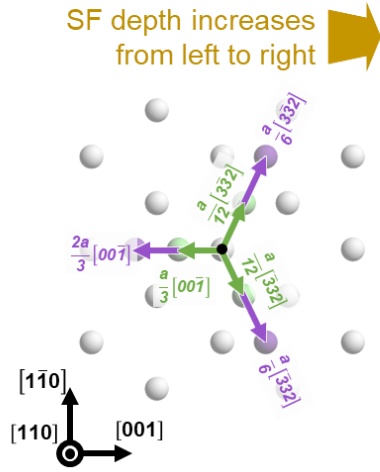
representing two-layer faults in Supplementary Fig. 1 are drawn in one crystal plane to visualize the total shifts between the upper and lower half crystal.

In the $L1_2$ structure (Supplementary Fig. 1b), the superstructure gives rise to additional distinctions between fault types based on whether nearest-neighbor violations (i.e., Al sites being unfavorably close to each other) exist between the fault planes. Intrinsic and extrinsic SFs still have the same effect on the stacking sequence as in the fcc structure. However, a Shockley partial now introduces a complex intrinsic SF (CISF, light green arrows) with additional nearest-neighbor violations. For a superlattice intrinsic SF (SISF, dark green arrows) without such violations, a twice as large $\frac{a}{3} \langle 211 \rangle$ Kear partial is required. Again, in both cases, this translation is possible in three different directions, and in the case of the SISF, all three translation directions lead to identical fault structures. On the other hand, the three CISF are crystallographically distinct, albeit only in their superstructure. Analogous to the fcc structure, a complex extrinsic SF (CESF, light purple arrows, also referred to as CESF-2) can be described as comprising two identical CISFs on neighboring planes. Similarly, a superlattice extrinsic SF (SESF, dark purple arrows) consists of two neighboring SISFs.

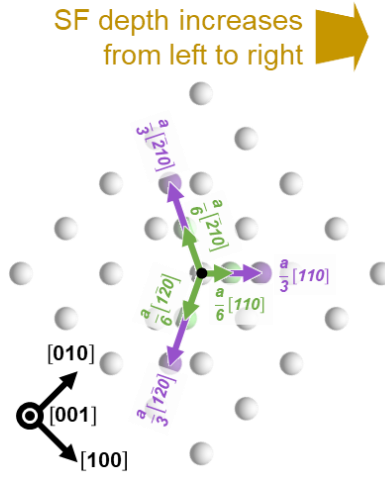
Supplementary Note 2: Projections of fault translation vectors along the [110] and [001] viewing directions.

For the projections of the net translation vectors of faults along the [110] and [001] viewing directions, the faults are considered to be situated on the (111) plane in accordance with Supplementary Fig. 1 and the main text, without loss of generality. Likewise, the structures in Supplementary Fig. 2 and Supplementary Fig. 3 are rotated so that the depth of the SF and its (111) habit plane increases from left to right. In [110] projection, this means that the [001] direction points to the right, whereas in [001] projection, the [110] direction points to the right.

a Projection into **[110] ZA**



b Projection into **[001] ZA**



Supplementary Fig. 2: Schematic illustration of the fcc crystal structure in (a) **[110]** and (b) **[001]** projection, with net translation vectors of ISF and ESF projected into the respective plane. The projected vectors correspond to those shown in Supplementary Fig. 1a, i.e., to a fault on the (111) plane. In accordance with the analysis presented in the main text, the structures are rotated so that the depth of the (111) plane inclined to the viewing direction increases from left to right.

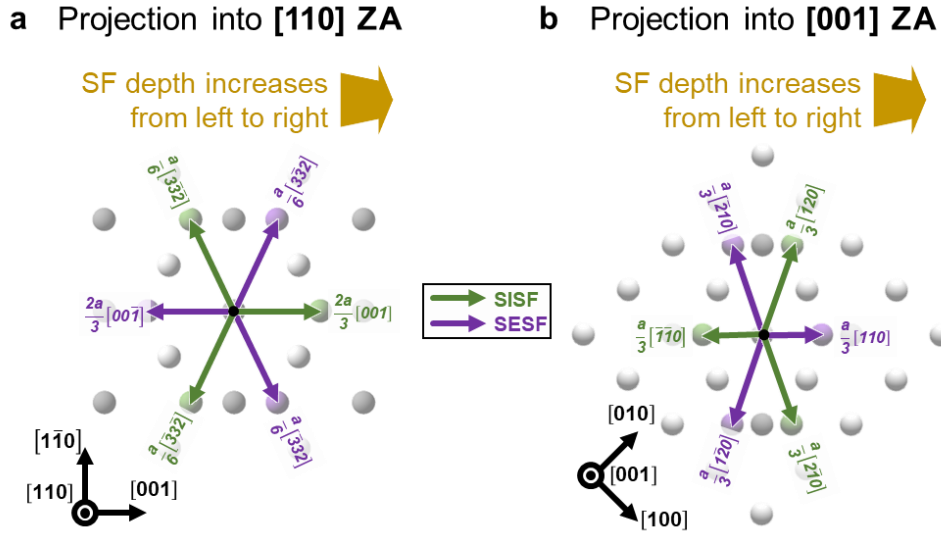
Projected net translation vectors of ISF and ESF in the **fcc structure** are shown in Supplementary Fig. 2.

In the **[110] ZA** (Supplementary Fig. 2a), the projections of the ISF translation vectors $a/6 [11\bar{2}]$, $a/6 [1\bar{2}1]$, and $a/6 [\bar{2}11]$ are $a/3 [00\bar{1}]$, $a/12 [3\bar{3}2]$, and $a/12 [\bar{3}32]$, respectively (for better distinction, projected vectors are written in italics). Since all three ISF translation vectors result in the same fault structure, the same holds true for the projected vectors (summarized as $a/3 [00\bar{1}]$ in the main text) and resulting structure, where the shifted lattice appears translated by one third of the periodicity “to the left” of the reference lattice.

The ESF translation vectors and thus their respective projections are twice as large. Again, the resulting three projected fault structures are identical (and summarized as $2a/3 [00\bar{1}]$ in the main text). Here, the shifted lattice appears “to the right” of the reference lattice.

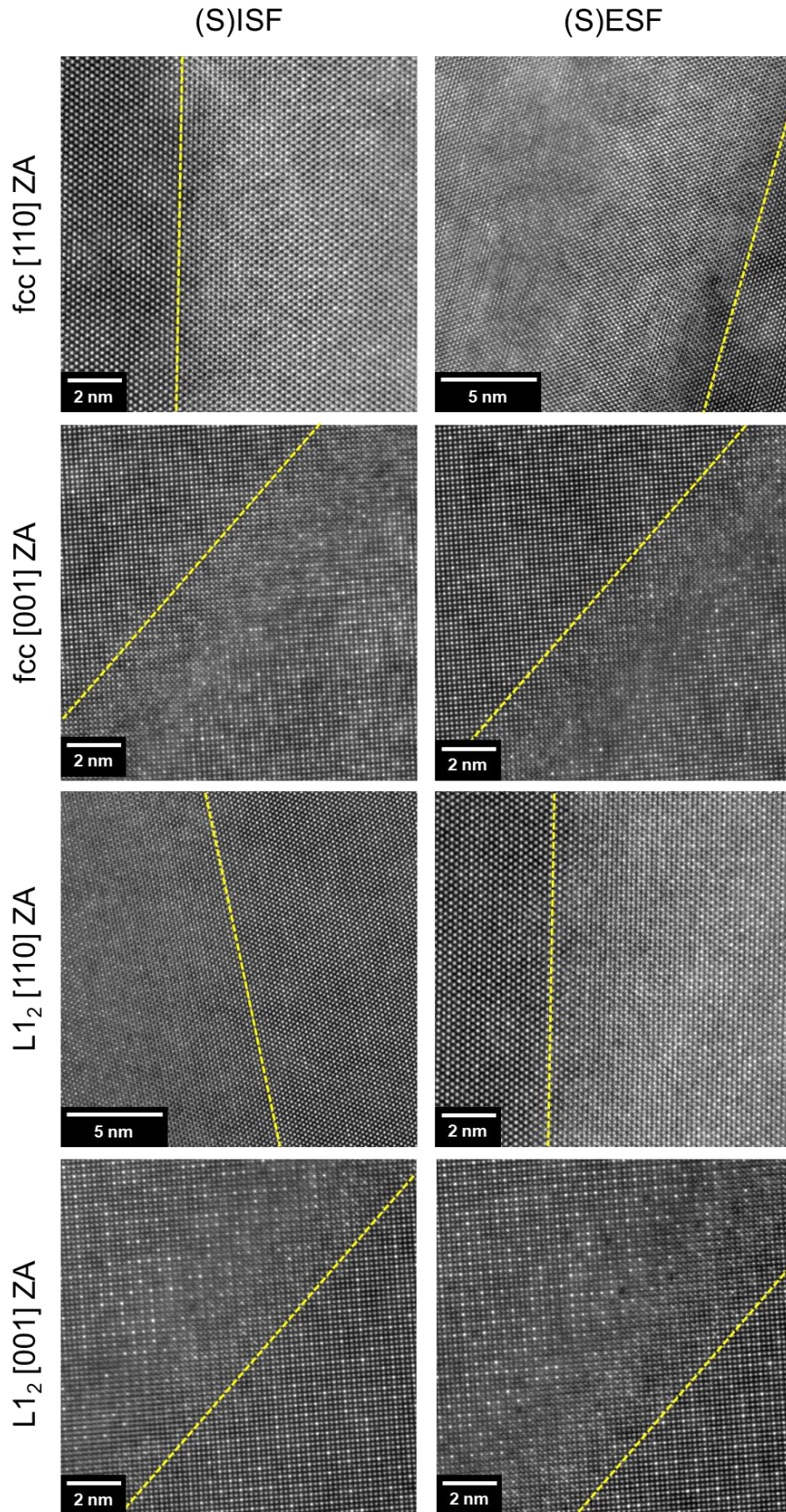
In the **[001] ZA** (Supplementary Fig. 2b), the ISF translation vectors $a/6 [11\bar{2}]$, $a/6 [1\bar{2}1]$, and $a/6 [\bar{2}11]$ have projections of $a/6 [110]$, $a/6 [1\bar{2}0]$, and $a/6 [\bar{2}10]$, respectively, with identical projected fault structures (the projected translation is summarized as $a/6 [110]$ in the main text). This means that the shifted lattice appears “to the right” of the reference lattice.

Again, the three translation vectors of ESFs and their projections are twice as large and the three projected structures identical (summarized as $\frac{a}{3} [110]$ in the main text) with the shifted lattice appearing “to the left” of the reference lattice.



Supplementary Fig. 3: Schematic illustration of the L_{12} crystal structure in (a) $[110]$ and (b) $[001]$ projection, with net translation vectors of SISF and SESF projected into the respective plane. The projected vectors correspond to those shown in Supplementary Fig. 1b, i.e., to a fault on the (111) plane. In accordance with the analysis presented in the main text, the structures are rotated so that the depth of the (111) plane inclined to the viewing direction increases from left to right.

Projections of SISF and SESF translation vectors in the **L_{12} structure** are illustrated in the same way in Supplementary Fig. 3. Compared to the ISF in the fcc structure, translation vectors of the SISF – and thus their projections in the $[110]$ and $[001]$ ZAs – are twice as large and antiparallel, also leading to projected fault structures where the shifted lattice appears “to the left” of the reference lattice in the $[110]$ ZA and “to the right” in the $[001]$ ZA. The net translation vectors of SESFs in L_{12} are identical to those of ESFs in fcc, and the same applies to their projections. In the projected fault structures, the shifted lattice appears “to the right” of the reference lattice in the $[110]$ ZA and “to the left” in the $[001]$ ZA.

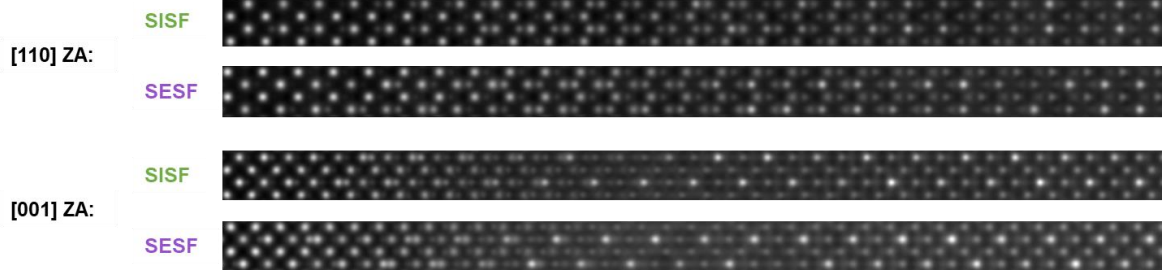


Supplementary Fig. 4: Micrographs from which the regions shown in Fig. 3 and 5 in the main text were extracted. The direction and approximate location of the respective fault's top edge is marked by a dashed yellow line.

a fcc structure



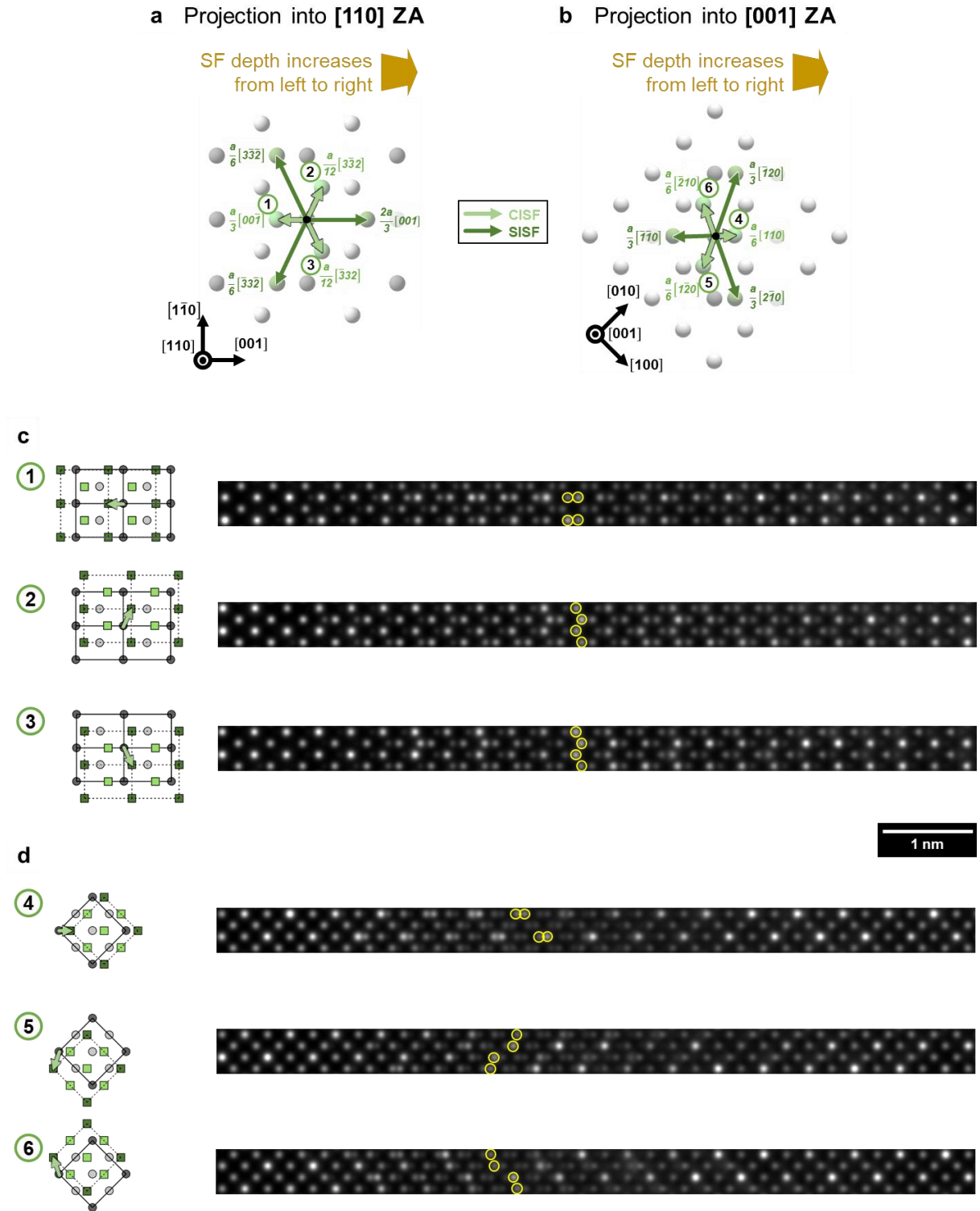
b L₁₂ structure



Supplementary Fig. 5: HAADF-STEM multislice simulations of inclined SFs for the different fault types. (a) fcc structure, corresponding to Fig. 2 and 3 in the main text. (b) L₁₂ structure, corresponding to Fig. 4 and 5 in the main text.

Supplementary Note 3: Projected structures of complex faults in the L₁₂ structure.

The difference between complex faults and their non-complex (superlattice) counterparts in the L₁₂ structure is only in the superlattice ordering, i.e., the stacking sequence of close-packed planes, ignoring the individual sublattices, is the same. Therefore, atomic columns also appear in the same positions in HRSTEM micrographs; differences in projected fault structures can only arise in terms of which atomic columns appear brighter or darker due to Z contrast.



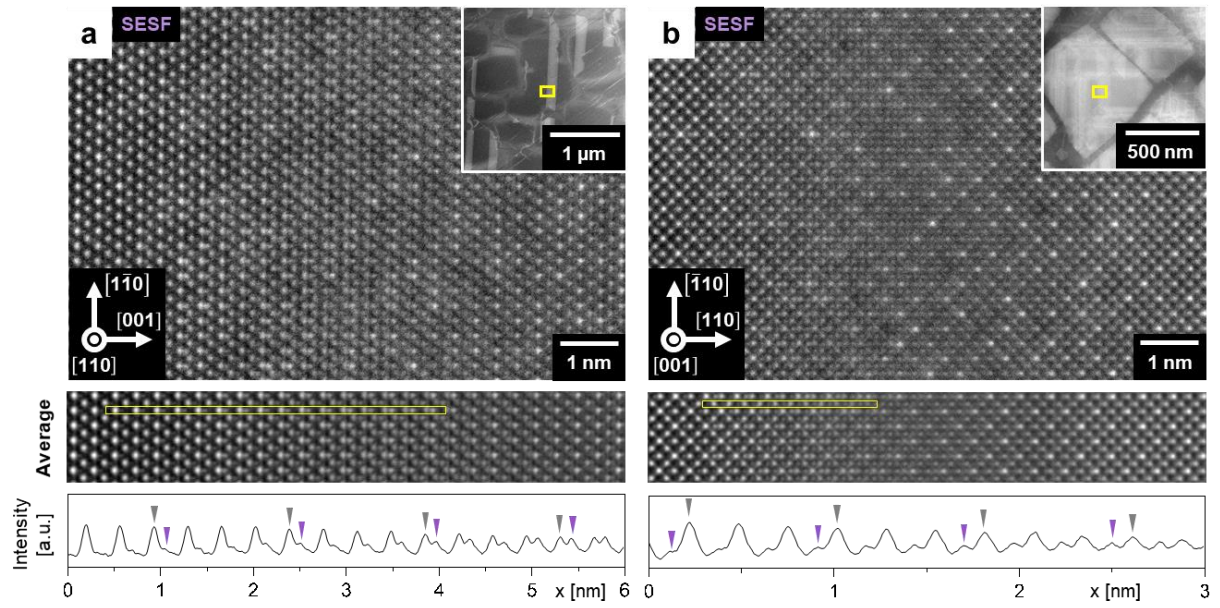
Supplementary Fig. 6: Schematic illustration of the L₁₂ crystal structure in (a) $[110]$ and (b) $[001]$ projection, with net translation vectors of CISF (and SISF for comparison) projected into the respective plane. The projected vectors correspond to those shown in Supplementary Fig. 1b, i.e., to a fault on the (111) plane. In accordance with the analysis presented in the main text, the structures are rotated so that the depth of the (111) plane inclined to the viewing direction increases from left to right. Below, projected structures and multislice image simulations (for a reduced sample thickness of 12 nm for enhanced superlattice contrast) corresponding to the different CISF translation vectors are shown for (c) $[110]$ and (d) $[001]$ projection.

The projected fault translation vectors of **CISFs**, along with **SISFs** for comparison, are presented in Supplementary Fig. 6 (cf. Supplementary Fig. 1b for the in-plane view of fault translation vectors) along with HAADF-STEM multislice simulations of the corresponding faults. Unlike their superlattice counterparts, the three possible translation directions result in crystallographically distinct fault structures, again differing only in their superstructure. Thus, all three are considered separately and numbered for reference.

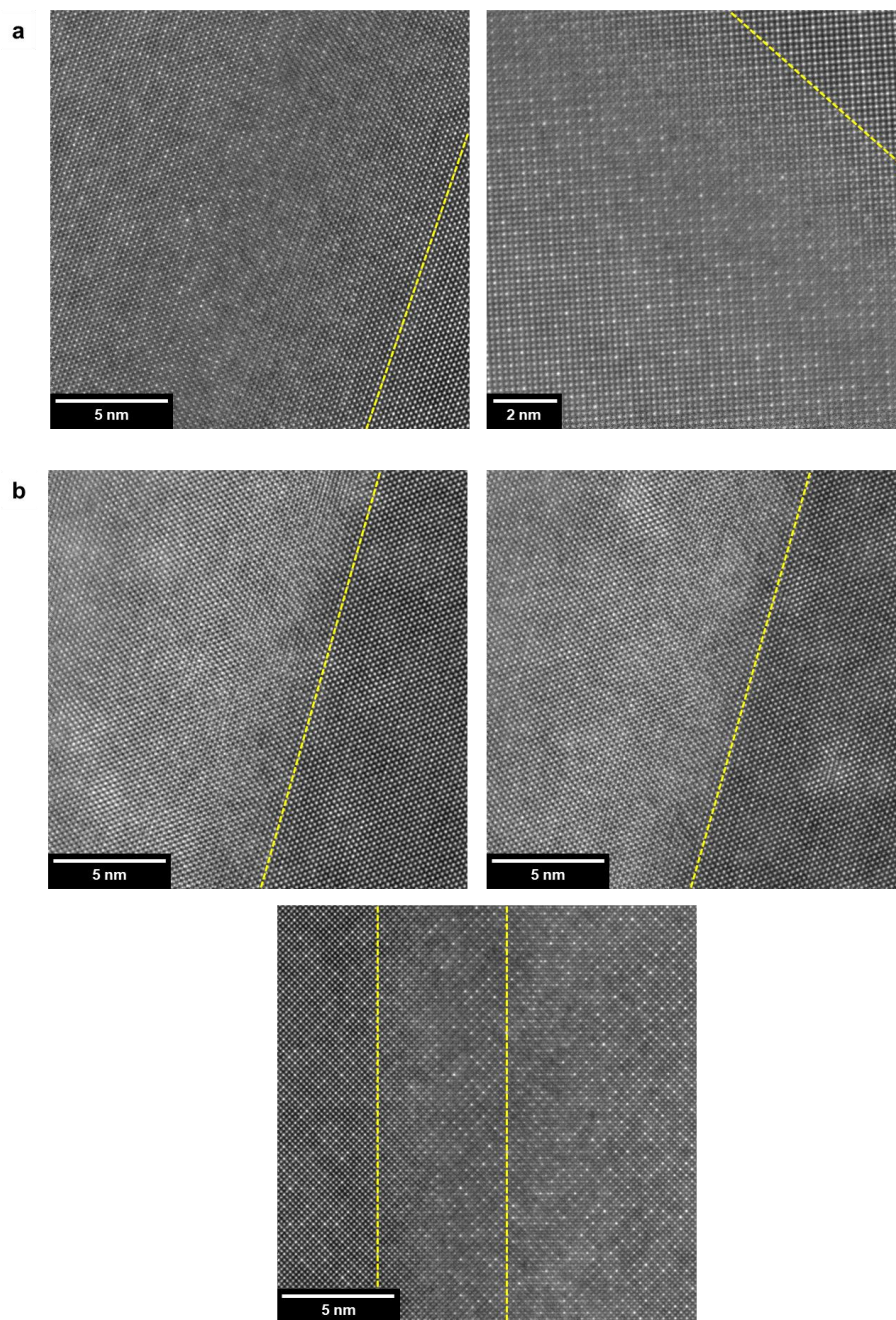
In the **[110] ZA** (Supplementary Fig. 6a), the projected fault translation vector of $a/3[00\bar{1}]$ results in a projected fault structure identical to that of an **SISF** (cf. Fig. 6 in the main text), where neighboring columns are of the same type and thus appear at the same brightness in HAADF contrast (Supplementary Fig. 6c). The projected translation vectors $a/12[3\bar{3}2]$ and $a/12[\bar{3}32]$, on the other hand, result in a different projected structure where mixed neighboring columns appear. Thus, only in these two cases, the **CISF** can unambiguously be identified as such. As a visual guide, brighter columns are highlighted by yellow circles.

A similar pattern emerges in the **[001] ZA** (Supplementary Fig. 6b,d): the projected structure associated with $a/6[110]$ is identical to that of the **SISF**, recognizable by the presence of $(1\bar{1}0)$ planes (i.e., horizontal rows) containing only one sublattice. The other two projected translation vectors, $a/6[1\bar{2}0]$ and $a/6[\bar{2}10]$, result in projected structures characteristic to the **CISF**.

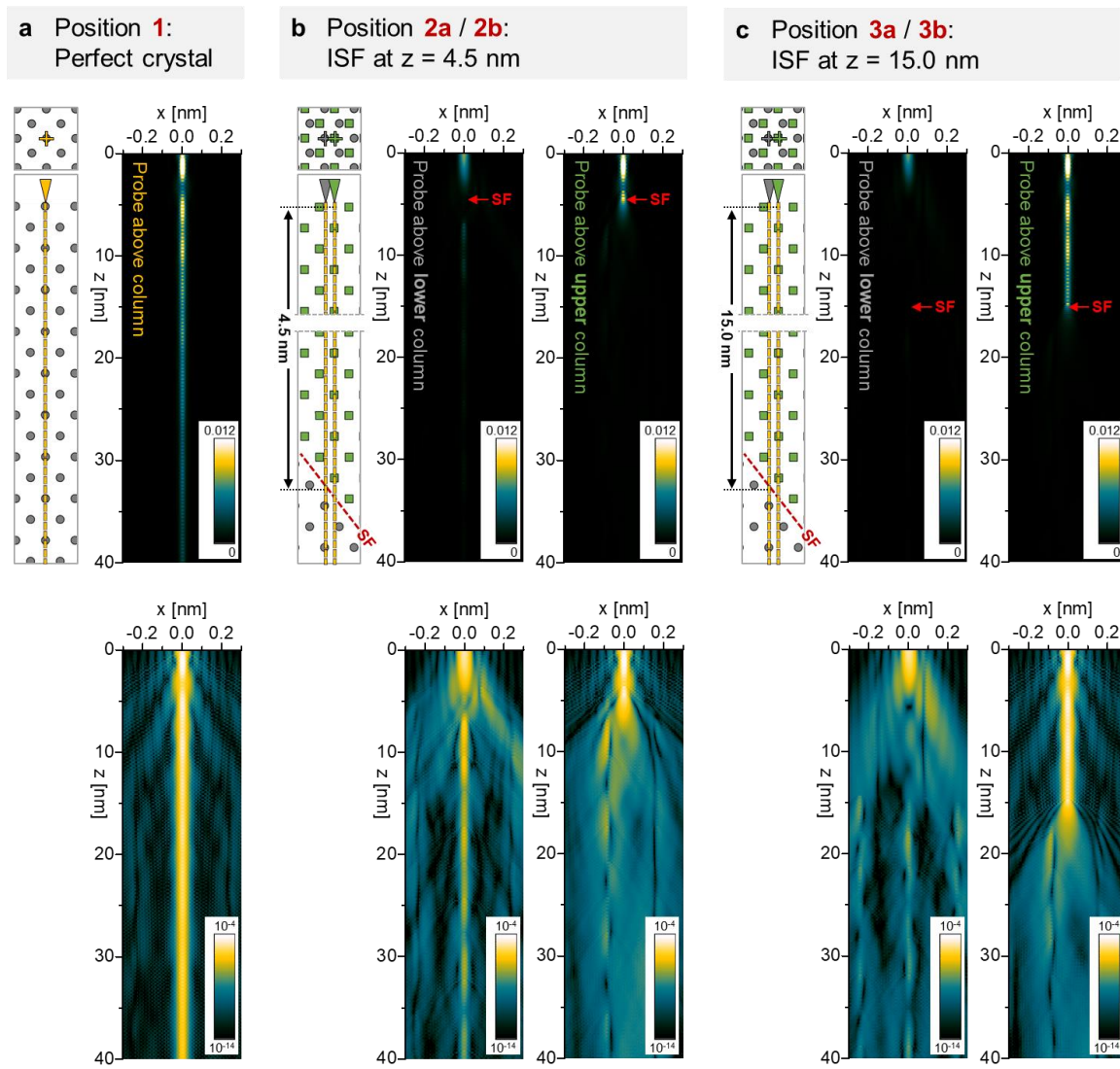
CESFs are not distinguishable at all from **SESFs** using the method presented in this work. This is because the contrast of projected fault structures almost only depends on the net translation vector of the imaged inclined fault, which is identical for **CESF** and **SESF** (cf. Supplementary Fig. 1b). Between the two fault structures, the superstructure only of the central fault plane is shifted. This difference within a single crystal plane has a negligible effect on image contrast.



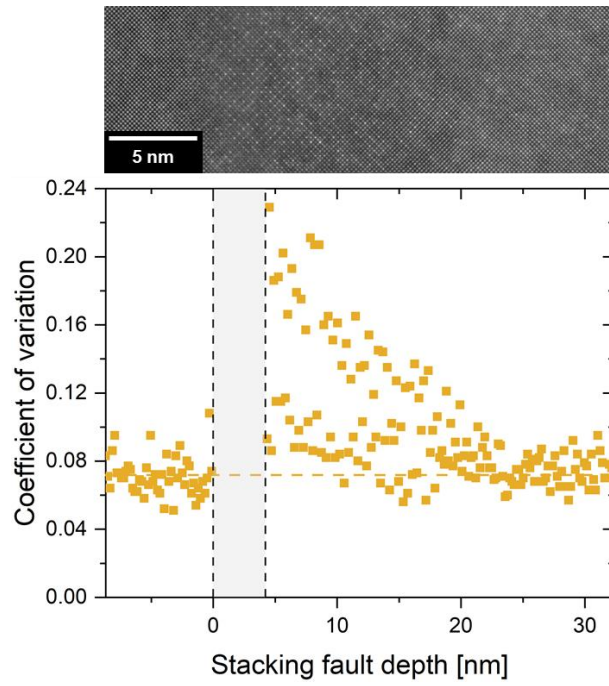
Supplementary Fig. 7: Analysis of SFs at high foil thickness. HRSTEM micrographs of SFs in the $L1_2$ structure (a) in the $[110]$ ZA at a thickness of approx. 100 nm and (b) in the $[001]$ ZA at a thickness of approx. 130 nm. The insets show ADF-STEM micrographs of the sample regions where the respective HRSTEM micrograph was recorded (yellow rectangle). The local foil thickness was calculated geometrically from the projected width of the SF as well as its inclination angle.



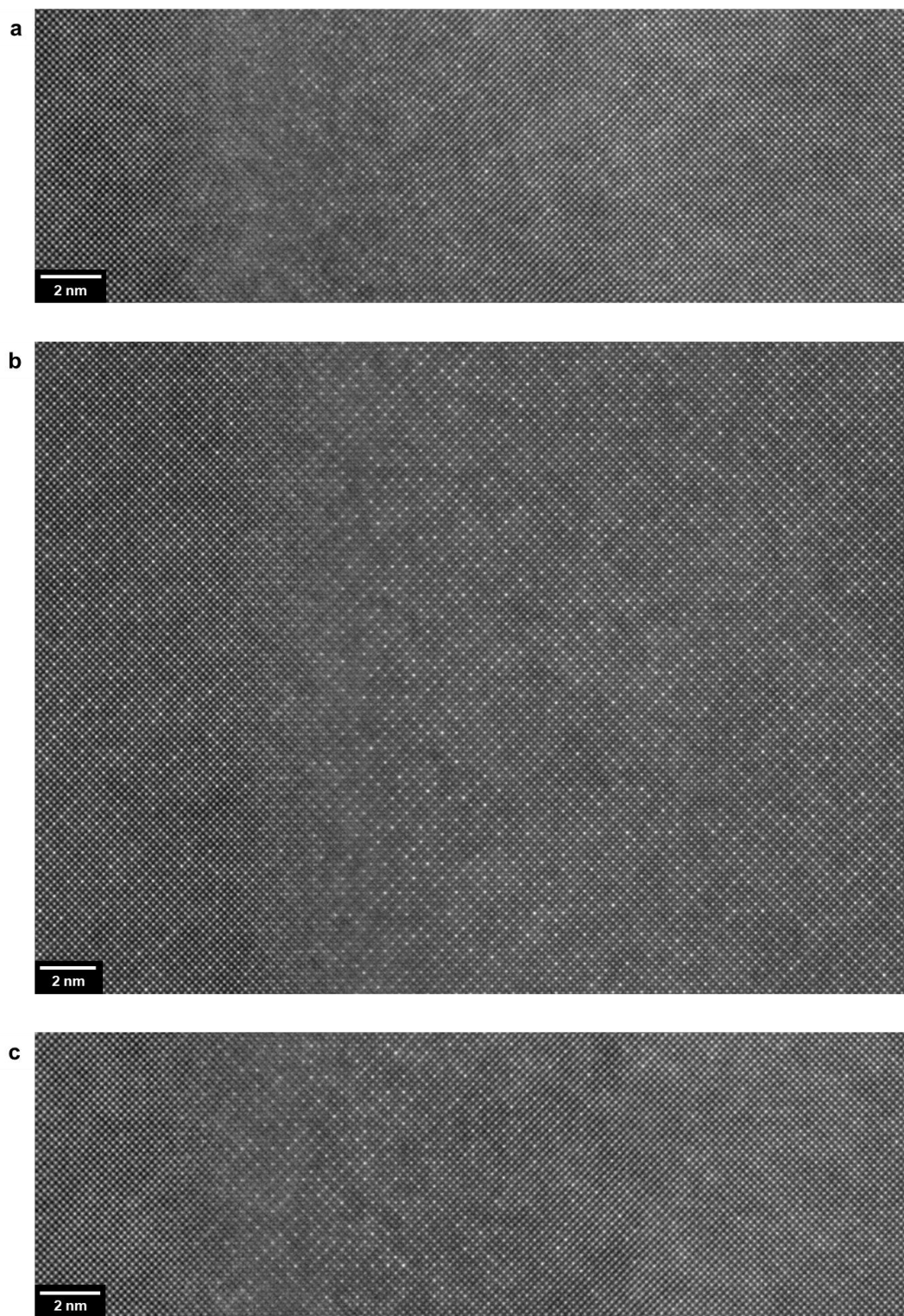
Supplementary Fig. 8: Micrographs from which the regions shown in Supplementary Fig. 7 (a) and Fig. 6 in the main text (b) were extracted. The direction and approximate location of the respective fault's top edge is marked by a dashed yellow line.



Supplementary Fig. 9: Linear (top) and logarithmic (bottom) presentation of the slices of simulated probe intensity distributions shown in Fig. 7 in the main text.



Supplementary Fig. 10: Analysis of enhanced Z-contrast above an inclined SF with a nano- γ' precipitate. HRSTEM micrograph of an inclined SF in the fcc structure. The plot below shows the CV of atomic-column intensities within each (220) plane. The horizontal line represents the baseline SD determined in a region of perfect lattice to the left of the SF. The HRSTEM image was stitched together from two separate micrographs to obtain a field of view containing regions to the left and right of the inclined SF. The full HRSTEM image on which the analysis was performed can be found in Fig. S11c.



Supplementary Fig. 11: HRSTEM images on which contrast analysis was performed. (a) fcc structure, see Fig. 8a in the main text. (b) L1₂ structure, see Fig. 8b in the main text. (c) fcc structure with nano- γ' precipitate, see Fig. S10.